ARTICLE

Glutathione-Exhausting Nanoprobes for NIR-II Fluorescence Imaging-Guided Surgery and Boosting Radiation Therapy Efficacy via Ferroptosis in Breast Cancer

Min Wei,[¶] Jingwen Bai,[¶] Xiao Shen, Kangliang Lou, Yiyang Gao, Ruichan Lv, Peiyuan Wang,* Xiaolong Liu,* and Guojun Zhang*

Read Online

ACCESS | Metrics & More | Article Recommendations | Supporting Information

ABSTRACT: Breast-conserving surgery (BCS) is the standard of care for early breast cancer patients, while the high ratio of reoperation is still a challenge due to inaccurate margin assessments. In patients with locally advanced or advanced breast cancer, radiotherapy is an important treatment for local control or improvement of quality of life. However, enhancing sensitization to radiotherapy is an unmet medical need. To solve the above clinical predicaments, a glutathione (GSH) exhausting virus-like silicon dioxide nanoprobe with Gd coating and folic acid (FA) modification is designed. After loading ICG in the mesopores, the VGd@ICG-FA probe efficiently targets tumor cells with high resolution, due to its virus-like morphology and folate acid anchoring. Especially, the fabricated nanoprobe enables the identification of tiny cancers and navigates precise surgery under NIR-II fluorescence imaging. Moreover, after the nanoprobes enter into the cytoplasm of cancer cells, tetrasulfide linkages in the silica framework are broken under the triggering of high GSH concentrations. In turn, the broken framework exhausts GSH to disrupt intracellular reactive oxygen species (ROS) homeostasis, and Gd produces more ROS under radiotherapy, further activating ferroptosis, and resulting in the enhancement of radiotherapy in breast cancer. Therefore, our nanoprobe exhibits tremendous potential as a NIR-II fluorescence imaging agent with no systematic side effects for precise cancer surgery and nanotherapeutics for boosting radiation sensitivity in future clinical translation of breast cancer.

KEYWORDS: GSH-exhausting, NIR-II fluorescence imaging, imaging-guided surgery, radiation sensitization, breast cancer
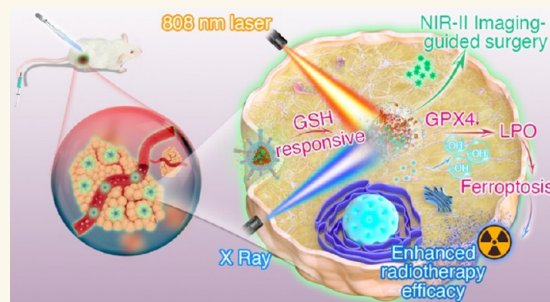
reast cancer has become the most commonly diagnosed malignant tumor globally.[1] Currently, most patients with stage 0 to II breast cancer, also called early stage breast cancer patients, are recommended to undergo breast-conserving surgery (BCS).[2] However, the reoperation rate for BCS ranges from 10 to 54% in America and 12−30% in the United Kingdom with a high risk of recurrence.[3−5] The main reason for the high reoperation rate is lacking effective means to display the tumor boundary intraoperatively, so the surgeons rely mainly on clinical experiences, like palpation and inspection which is prone to misjudgment. Although intraoperative frozen section analysis and imprint cytology are conducive to diagnosing positive margins, they cannot reflect the intact tissue and have 5−15% discrepancies with permanent pathology after surgery.[6] Consequently, it is crucial to develop methods for accurately identifying margins when performing BCS. Fluorescence imaging of near-infrared light in

the first window (NIR-I, 650−900 nm) provides a modality for precise surgical navigation in real-time.[7,8] Besides, the NIR-I fluorescence imaging-guided surgery can assist to find the residual tumor tissues in the whole section surface.[9] However, the clinically used fluorophores, such as 5-aminolevulinic acid (5-ALA),[10] methylene blue (MB),[11] and indocyanine green (ICG),[12] have some restrictions such as photobleaching,[13] short blood half-life,[14] and nonspecific targeting properties.[15,16] Especially, the poor penetration depth and low tumor-to-background ratio (TBR) are insufficient for deep tissue
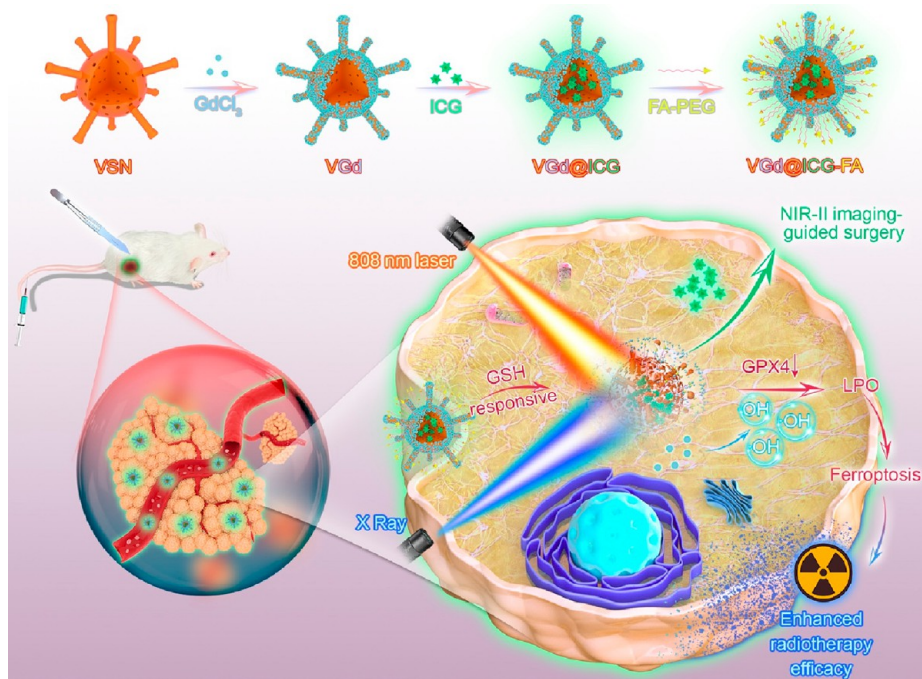
Figure 1. Schematic illustration of VGd@ICG-FA nanoprobe fabrication for NIR-II fluorescent image-guided breast cancer surgery and ferroptosis enhanced radiosensitization.

imaging.[17] It is sorely urgent to generate a probe with relatively longer-wavelength fluorescence emission, tumor-specific targeting, and antiphotobleaching properties.

The second near-infrared region (NIR-II, 1000–1700 nm) can significantly reduce scattering and biological tissue autofluorescence, enabling deeper and high-fidelity optical tumor imaging.[18] Although ICG has off-peak emission spectra in NIR-II and has been extensively explored for surgical navigation, the lack of antiphotobleaching and tumor tissue recognition abilities are still concerning.[19,20] According to our previous work, ICG loaded into mesopores of the nanocarriers could substantially increase the antiphotobleaching performance.[21] Heretofore, up to 13 clinical studies have confirmed the biosafety and efficacy of mesoporous silica nanoparticles (MSN) for drug delivery, diagnostics, and therapeutics in humans,[22] and silica nanoparticles can increase the bioavailability of drugs by up to 3.5 times.[23,24] Specifically, after loading ICG into the mesopores of MSN, the fluorescence self-quenching effect can be attenuated.[25] Meanwhile, virus-like silica nanoparticles with excellent adhesion to cell membranes and tumor retention are becoming the research priorities.[26,27] Since the folic acid receptor (FOLR1) was highly expressed in breast cancer,[28,29] we synthesize an advanced virus-like mesoporous silicon with folic acid (FA) modification for precise delivery of ICG for real-time discrimination of positive margins in BCS.

Additionally, radiation therapy (RT) is often used for the palliative treatment of patients with advanced breast cancer in recent years. However, owing to the low sensitivity to RT, 56% of advanced breast cancer patients metastasize 14 months after radiotherapy.[30] Moreover, it gives an insufficient irradiation dose to damage tumors due to the limitation of normal tissue tolerance dose.[31,32] Hence, the enhanced sensitivity to radiation and precise RT are prominent directions in clinical practice. Ferroptosis has been preliminarily explored to be closely related to the sensitivity of radiotherapy and this effect

can be eliminated by ferroptosis inhibitors.[33−35] Ferroptosis is defined as programmed cell death based on lipid peroxidation (LPO) which is directly induced by reactive oxygen species (ROS).[36,37] It has three main properties: high ROS levels,[36] low glutathione (GSH) concentration and glutathione peroxidase 4 (GPX4) expression,[38] and LPO initiated by high ROS.[39] Because of the high atomic number element gadolinium (Gd), which possesses a larger X-ray photon capture cross section and Compton scattering effect, Gd-loaded MSN is a good RT sensitization strategy to excessively produce intracellular ROS upon radiation exposure.[40] Meanwhile, high levels of GSH can be detected in tumor cells, which is about 10−1000-fold higher than in normal cells.[41] MSN containing tetrasulfide bonds are able to deplete intracellular GSH content and increase the ROS level by GSH redox.[42] Thereby, it would be ideal to design an effective Gd and tetrasulfide composite MSN that presents GSH exhausting capability and ROS generating capacity for maintaining high ROS in cancer cells, so that the ROS induced by two ways can adequately mediate LPO and thus achieve greater sensitivity to RT.

Herein, our present study aimed to design a multifunctional nanoprobe that is able to guide BCS of early stage breast cancer and boost the radiotherapy sensitization efficacy via ferroptosis of advanced breast cancer. As shown in Figure 1, we successfully synthesized a Gd-coated and tetrasulfide bonds doped mesoporous virus-like SiO_2 nanoprobe with surface modification of FA (VGd@FA). Encapsulating ICG within nanoprobes (VGd@ICG-FA) effectively delayed the time of photobleaching, which led to a stable imaging effect for ICG to guide surgical navigation. The virus-like morphology enabled potent tumor cell adhesion and enhanced cellular uptake efficiency. After intravenous injection into the tumor-bearing mice, it could also be precisely concentrated in the tumor site and brought a higher TBR than that of ICG alone (8.26 ± 0.83 vs 1.76 ± 0.06, $p < 0.0001$). In addition, this probe successfully
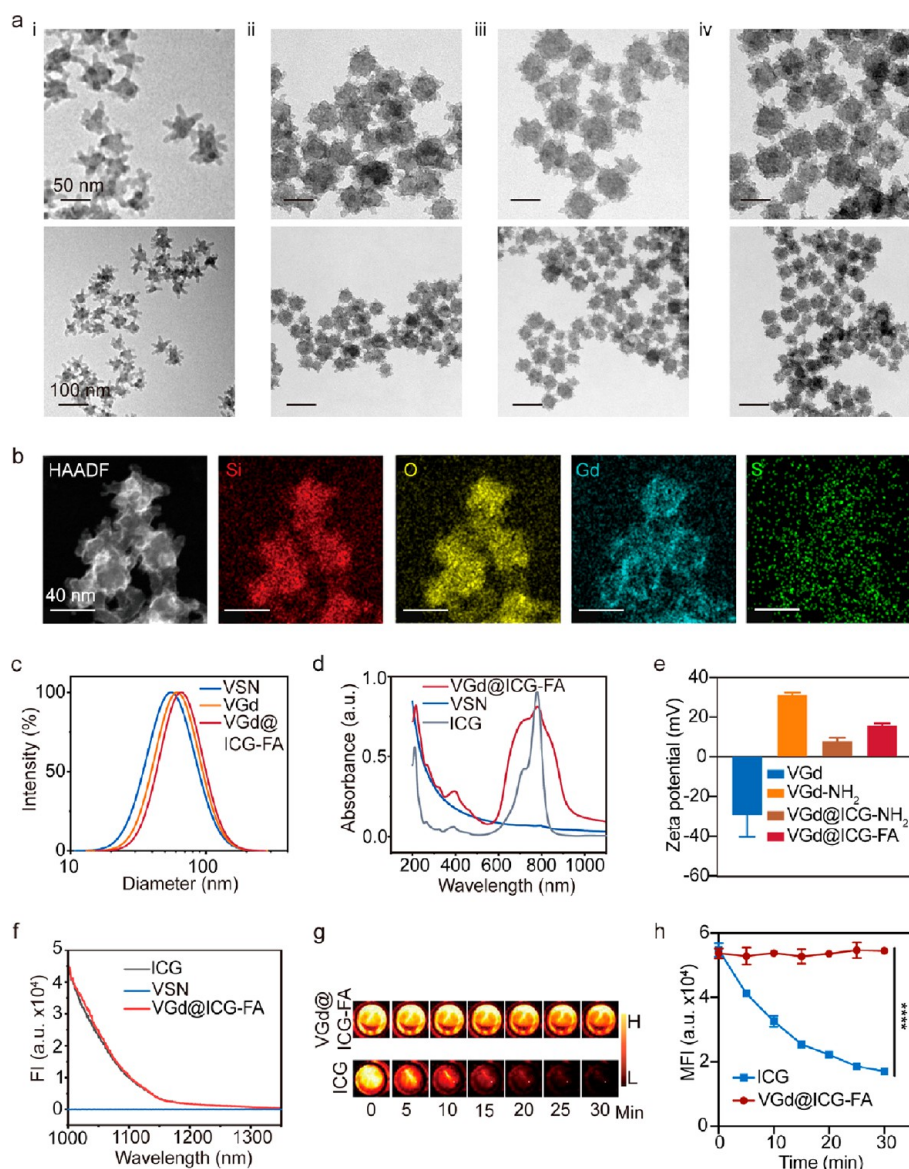
Figure 2. Characterization of nanoprobes. (a) TEM images of VSN (i), VGd (ii), VGd@ICG-NH$_2$ (iii), and VGd@ICG-FA (iv). (b) HAADF-STEM image and element mappings of VGd. (c) Diameter distribution of VSNs, VGd, and VGd@ICG-FA. (d) UV−NIR absorption spectrum of ICG, VSN, and VGd@ICG-FA. (e) Zeta potential changes on the process of synthesis of VGd@ICG-FA. (f) Fluorescence emission spectrum of ICG, VSN, and VGd@ICG-FA. (g) NIR-II fluorescence images of ICG and VGd@ICG-FA under continuous irritation of 808 nm laser. (h) The corresponding quantitative statistics of mean fluorescence intensity in g. The data are shown as the mean ± SD (*p < 0.05, **p < 0.01, ***p < 0.001, ****p < 0.0001).

guided the precise resection in multiple breast cancer models with the complete removal of at least 1 mm^3 solid tumors. Besides, the doped tetrasulfide linkages reduced the GSH concentrations in tumor cells, which in turn induced ferroptosis. Most importantly, VGd@ICG-FA boosted the radiation therapy efficiency via ferroptosis, specifically with GSH depletion, GPX4 downregulation, ROS accumulation, and LPO activation. Furthermore, safety indicators showed that our nanoprobes did not bring significant safety concerns. Our findings show the multifunctional GSH-depleted nanoprobe's significant potential for promoting the accuracy of tumor excision under NIR-II fluorescence imaging-guided BCS and improving RT sensitization through ferroptosis in breast tumor ablation.

RESULTS

Synthesis and Characterization of VGd@ICG-FA. As schematically illustrated in Figure 1, VGd@ICG-FA was synthesized in an oil/water reaction system and further underwent Gd$_2$O$_3$ coating, ICG loading, and FA modification. First, virus-like tetrasulfide bonds doped silica nanoparticles (VSNs) were synthesized in a biphase reaction system with hexadecyltrimethylammonium bromide (CTAB) as a structural template. Here, a mixture of tetraethyl orthosilicate (TEOS) and bis[3-(triethoxysilyl)propyl]tetrasulfide (BTES) was used (weight ratio TEOS:BTES = 8:1) as the tetrasulfides doped silica precursor, and NaOH was set as a catalyst. Thus, VSNs with GSH-exhausting ability were successfully synthesized after 72 h stirring at 60 °C. Transmission electron microscopy (TEM) images of obtained nanoparticles clearly demonstrated that monodispersed VSNs had virus-like
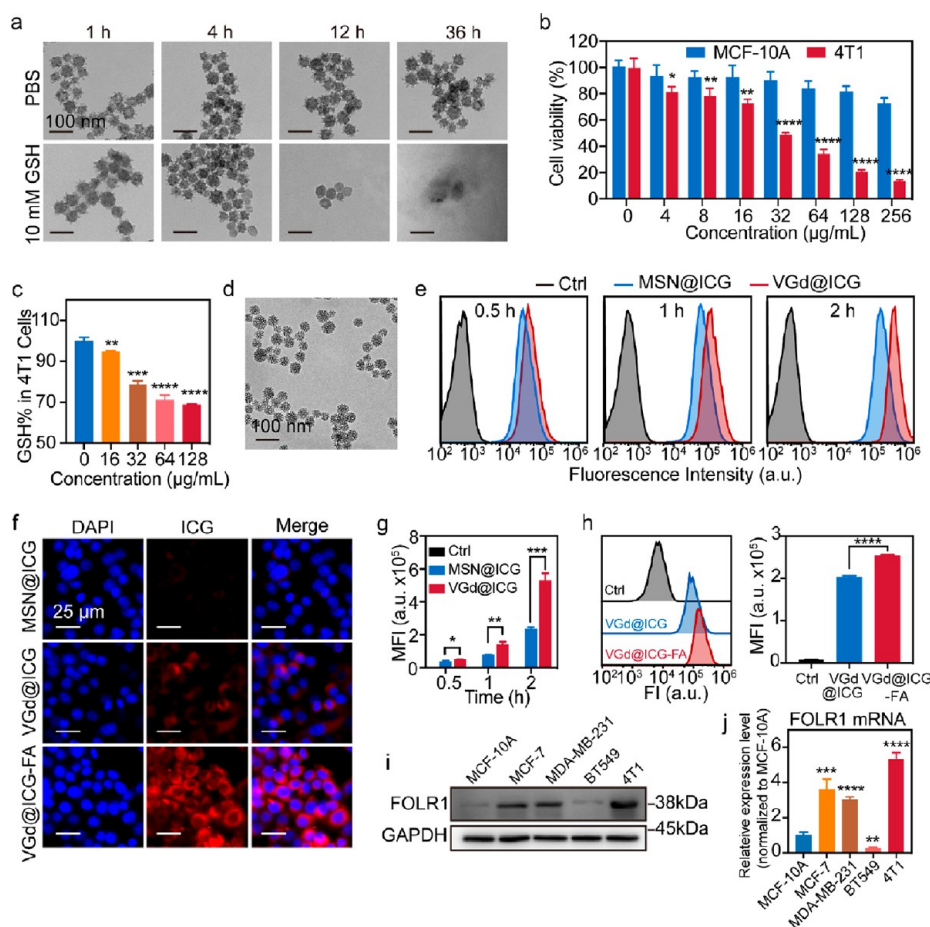
Figure 3. GSH-responsive and cellular uptake of VGd@ICG-FA nanoparticles. (a) TEM images of VGd@ICG-FA immersed in PBS or 10 mM GSH solution for various durations. (b) Cell viability analysis of MCF-10A and 4T1 cells incubated with VGd@ICG-FA of a series of concentrations. (c) GSH concentration in 4T1 cells after incubation with VGd@ICG-FA at various concentrations. (d) TEM image of MSN@ICG. (e) Flow cytometry results of 4T1 cells after incubation with MSN@ICG or VGd@ICG at different time points, respectively. (f) The CLSM results of 4T1 cells after being treated with MSN@ICG, VGd@ICG, and VGd@ICG-FA for 2 h. (g) The corresponding quantitative statistics of mean fluorescence intensity in e. (h) Flow cytometry analysis of 4T1 cells after incubated with VGd@ICG and VGd@ICG-FA for 4 h (left) and the corresponding quantitative statistics of mean fluorescence intensity (right). WB results (i) and mRNA expression levels (j) of FOLR1 expression in normal breast epithelial cells and different breast cancer cell lines. The data are shown as the mean ± SD (*$p < 0.05$, **$p < 0.01$, ***$p < 0.001$, ****$p < 0.0001$).

morphology with a uniform size of ∼56 nm (Figure 2a-i). Then, Gd_2O_3 was successfully wrapped on VSNs after a 12 h reaction under the presence of a reducing agent (hexamethylenetetramine) with $GdCl_3·6H_2O$ as the Gd-based precursor. Scanning electron microscopy (SEM) image showed that VGd preserved the virus-like rough morphology (Figure S1). Obviously, the TEM image displayed the Gd deposition on the surface of well-dispersed VGd (Figure 2a-ii). The element distribution results of VGd proved that homogeneous Si, O, Gd, and S elements were distributed throughout the entire outside architecture of the nanoparticles (Figure 2b). Moreover, according to Inductively Coupled Plasma Optical Emission Spectrometry (ICP-OES) analysis, the Gd concentration was calculated as 16%. Besides, from energy-dispersive X-ray spectroscopy (EDS) data, the mass fraction ratio of Si, Gd, and S was determined as 35.82:15.89:0.21 (Table S1). These results demonstrated that Gd_2O_3 and tetrasulfide bonds were successfully wrapped and codoped in the VSNs, respectively. Furthermore, to facilitate the following modification, VGd was amino-modified by using amino silane, (3-aminopropyl)triethoxisilane (APTES) (VGd-NH$_2$). After that,

ICG was capsuled in VGd and the loading capacity was 10.26% (w/w%) by referencing the standard calibration of ICG (Figure S2). To confer tumor targeting ability to the nanoparticles, FA was anchored on the VGd surface by a common 1-(3-(dimethylamino)propyl)-3-ethylcarbodiimide hydrochloride (EDC)/N-hydroxysuccinimide (NHS) reaction (VGd@ICG-FA). During the synthesis process, VGd, VGd@ICG, and VGd@ICG-FA were evenly dispersed in water (Figure S3). During the ICG loading and FA motifs anchoring, the obtained VGd@ICG-FA maintained a viral appearance throughout (Figure 2a-iii, iv). Dynamic laser scattering analysis suggested that the size of VSN, VGd, and VGd@ICG-FA increased from ∼56 nm to ∼66 nm, verifying the successful construction of VGd and VGd@ICG-FA step by step (Figure 2c). UV−vis−NIR absorption spectrum analysis of VGd@ICG-FA and ICG exhibited the same characteristic peak at 780 nm, demonstrating that ICG had been successfully loaded into the mesopores (Figure 2d). In the Fourier transform infrared (FT-IR) spectrum of VGd@ICG-NH$_2$, the C=C skeletal vibrational of the benzene ring of ICG appeared at 1623, 1512, and 1420 cm^{-1}, indicating that ICG was successfully loaded

(Figure S4). In addition, after FA modification, the absorbance significantly increased from 600 to 800 nm, suggesting the efficient modification of FA (Figure 2d). Moreover, the zeta potential of VGd-NH$_2$ dramatically increased from -29.46 ± 10.84 to 31.25 ± 1.21 mV, while after ICG loading, it decreased appreciably (Figure 2e). Similar NIR-II spectral characteristics were seen in both VGd@ICG-FA and ICG when an 808 nm laser illumination was utilized with 1000 nm long pass filters (Figure 2f). All the above findings suggested the successful ICG loading and surface anchoring of FA in our prepared silica-based NIR-II nanoprobes.

Since ICG is unstable and has a quenching effect in aqueous solutions,[43] we explored whether loading it in the mesopore of VGd would increase its stability and antiquenching property. By measuring the absorption spectra several times within 96 h under daylight exposure, the ICG aqueous solution only remained at 8% of its fluorescence intensity, whereas VGd@ICG-FA still presented 89% fluorescence intensities (Figure S5). These results revealed the exceptional photostability of ICG encapsulation in VGd@ICG-FA, laying the solid foundation for subsequent bioapplications. Further, after continuous irradiation of ICG and nanoprobes by an 808 nm laser, ICG was quickly quenched with over 30% of its initial fluorescence intensity within 30 min. While VGd@ICG-FA remained at more than 98% of its intensity (Figure 2g, h). These results verified that nanoprobes could notably provide an antiquenching effect of ICG, which made the probe suited for long-term fluorescence imaging-guided surgical navigation and precise radiotherapy monitoring.

GSH-Responsive and Cellular Uptake of VGd@ICG-FA. Next, we studied the degradation tendency of tetrasulfide bonds in the mesoporous framework under a simulated tumor environment (10 mM GSH). TEM images recorded that at 4 h incubation, some of the spine structures of VGd@ICG-FA became shorter with most of the nanospikes disappearing after 12 h incubation with GSH. The core−shell nanoparticles wholly degraded at 36 h (Figure 3a), while no apparent counterparts decomposed in normal conditions during the whole incubation period, demonstrating the biodegradable capability under GSH triggering. Meanwhile, the release profiles of ICG and Gd^{3+} from VGd@ICG-FA were investigated. The nanoprobes were added into the solutions with 3 μM or 10 mM GSH at 37 °C to simulate the plasma and tumor intracellular environment, respectively.[44,45] ICG released rapidly in 10 mM GSH solution, achieving a maximum release of 68.58% at 36 h (Figure S6). In contrast, the ICG release rate was slow in the 3 μM GSH environment, with only 7.47% release at 56 h in the end. Similarly, undetectable Gd^{3+} was released in the low GSH environment. Undoubtedly, these findings verify that electrostatic interaction between the Gd$_2$O$_3$ shell and VSNs is particularly stable in stimulated physiological buffer. Furthermore, the released concentration of Gd^{3+} approximately reached the plateau level at 36 h incubation with high GSH buffer. Therefore, the above results confirmed that the tetrasulfide bonds in the probe framework could be broken under a high concentration of GSH, which realized the nanoprobe's high targeted release ability in the tumor environment.

Before the bioapplication, cell viabilities of normal and tumor cells were explored after coculturing with the prepared nanoprobes. Notably, the synthesized VGd@ICG-FA effectively decreased the viability of the breast cancer cell line (4T1 cells) by 51.4% at 32 μg/mL. In comparison, the normal

mammary epithelial cells (MCF-10A cells) only presented 9.8% inhibition, demonstrating the high cell killing efficiency of VGd@ICG-FA toward tumor cells and no obvious side effects to normal cells (Figure 3b), which laid the solid foundation for further animal experiments. Surprisingly, the cell viability study showed that VGd@ICG-FA− (nontetrasulfide doping) (Figure S7a) had little influence on the cell viability of tumor cells. When the concentration increased to 256 μg/mL, the cell survival rate of VGd@ICG-FA− was 4-fold higher than VGd@ICG-FA (Figure S7b). This was mainly due to the effective oxidative homeostasis disruption of VGd@ICG-FA that induced intracellular GSH depletion and eliminated tumor cells via ferroptosis.

GSH is an essential endogenous antioxidant that balances cellular activity and signal transduction pathways.[46] GSH depletion efficiently disrupts redox balance, thus elevating LPO generated by intracellular ROS increasing and finally inducing ferroptosis.[39] The effect of VGd@ICG-FA on GSH depletion promoted by the broken tetrasulfide bonds was investigated in the 4T1 tumor cells. As shown in Figure 3c, when 4T1 cells were introduced with 16 μg/mL VGd@ICG-FA for 36 h, the intracellular GSH concentration decreased by 5.05%. Notably, when the nanoprobe was administrated at 128 μg/mL, GSH concentration drastically dropped to 68.83%. The depletion of the intracellular GSH ability of our nanoprobe enabled it to be more useful for the disruption of redox homeostasis in tumor cells and mediate ferroptosis for triggering tumor cell death. Subsequently, we synthesized ICG-loaded mesoporous silicon nanoparticles (MSN@ICG) as the control to explore the benefits of virus-like morphology for cell membrane adherence. The TEM results confirmed that the particle size of MSN@ICG was comparable to that of VGd@ICG (∼60 nm) (Figure 3d). The cellular uptake of VGd@ICG was significantly higher than MSN@ICG after 0.5 h incubation (Figure 3e, g), and the fast internalization rate could be attributed to the unique topological structure.[47] Confocal laser scanning microscopy (CLSM) results also found that weaker red ICG signals were observed in the MSN@ICG group at 2 h than that in the VGd@ICG group (Figure 3f). Thus, all results proved the enhanced cell uptake efficacy of VGd@ICG with a virus-like appearance.

It has been published that folate receptor 1 (FOLR1) is highly expressed in numerous cell lines including breast cancer.[28,29] To explore if FOLR1 could be the target for breast cancer, the expression of FOLR1 was investigated in four representative breast cancer cell lines and normal breast cells MCF-10A. As expected, Western blot analysis and real-time qPCR results showed that murine 4T1, human MCF-7, and MDA-MB-231 cell lines highly expressed FOLR1 at both protein and mRNA levels (Figure 3i, j), demonstrating that FOLR1 had the potential as an important breast cancer target. It was found that compared with VGd@ICG, the uptake of VGd@ICG-FA in 4T1 cells at 2 h increased sharply (Figure 3f, h), demonstrating that the FA modification could further facilitate nanoparticle internalization. The specific affinity for tumor cells via virus-like nanostructure and FA modification primarily ensured the targeting ability *in vivo* for the following tumor surgery and radiotherapy.

***In Vivo* Targeted NIR-II Fluorescence Imaging.** Since the nanoprobe had the property of outstanding targeting capability toward breast cancer cells, we then validated the targeting of VGd@ICG-FA *in vivo* using the transplant 4T1 tumor mouse model. After intravenous injection of the VGd@
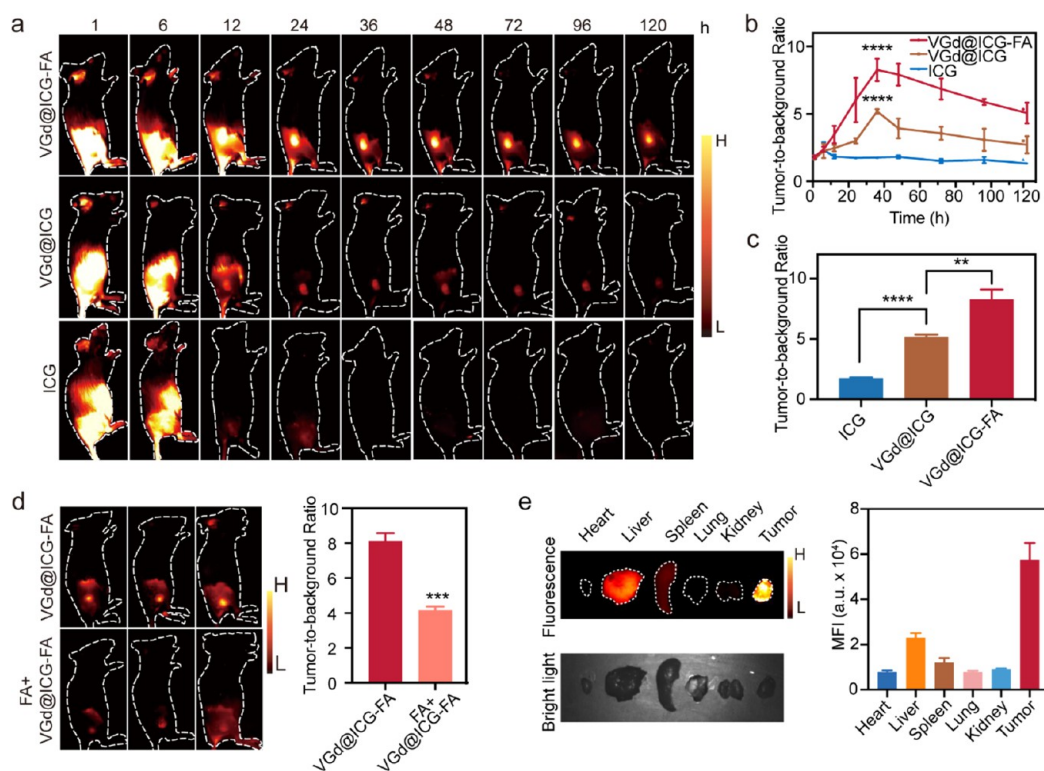
Figure 4. *In vivo* targeted fluorescent images of nanoprobes in breast tumor-bearing BALB/c mice. (a) Selected time points from NIR-II fluorescent images of 4T1-Luc bearing mice after injected with VGd@ICG-FA, VGd@ICG, and ICG ($n = 3$). (b) The corresponding quantitative statistics of tumor-to-background ratio in a. (c) Comparison of the specific tumor-targeting capacities of VGd@ICG-FA, VGd@ICG, and ICG at maximal TBR (36 h). (d) NIR-II fluorescent images of the 4T1-Luc tumor-bearing mouse with or without FA block before injecting VGd@ICG-FA (left) and the corresponding quantitative statistics of tumor-to-background ratio (right). (e) NIR-II fluorescence images (left) of organs and tumor excised 36 h after VGd@ICG-FA injection and quantitative fluorescent intensity analysis (right). The data are shown as the mean $\pm$ SD (*$p < 0.05$, **$p < 0.01$, ***$p < 0.001$, ****$p < 0.0001$).

ICG-FA nanoparticles into subcutaneous tumor-bearing mice, the tumor fluorescence could be seen in 1 h, then the outline of the tumor was clearly delineated within 36 h. The fluorescence signal gradually attenuated and lasted for 120 h postinjection which could be ascribed to the cell adhesion ability of our nanoprobes (Figure 4a, b). All fluorescence signal in tumor tissues in the VGd@ICG-FA group was profoundly higher than that of the VGd@ICG group, suggesting the active tumor recognition ability of FA. Furthermore, the peak TBR of 8.26 ± 0.83 at 36 h in the VGd@ICG-FA group was ultimately discovered, significantly higher than that of VGd@ICG groups (5.19 ± 0.17) (Figure 4c). This result coincided with the total biodegradation time in Figure 3a, reflecting the reliability of VGd@ICG-FA for pinpointing tumor location. Considering the highest TBR at 36 h, all the following *in vivo* surgeries and treatments were performed at this time point. In contrast, ICG was totally metabolized within 36 h on account of its short biological blood half-life and lack of tumor targeting capability (Figure 4a, b). Tumor targeting *in vivo* was further confirmed by preinjection of a blocking dose of the FA before the VGd@ICG-FA treatment. In this case, feebler tumor fluorescence could be observed owing to FA blocking ($p < 0.0001$). Nonspecific uptake of VGd@ICG-FA brought about the highest TBR of 4.16 ± 0.21 at 36 h postinjection (Figure 4d). Since most of the FDA-approved MRI contrast agents utilize Gd to produce an increased signal on T_1-weighted images,[48] in addition to the NIR-II fluorescence imaging, we further verified the targeting ability of our nanoprobes using MRI. Both MRI signals from VGd@ICG-FA and the clinical contrast

agent Gadoteric Acid Meglumine (GAM) groups significantly enhanced under a 1.5 T magnetic field. GAM showed the highest MRI signal in tumor tissue at 1 h postinjection, while VGd@ICG-FA peaked at 36 h and maintained signal intensity over 96 h, implying the great potential of VGd@ICG-FA for MRI-mediated tumor diagnosis (Figure S8a, b). Particularly, the highest TBR of VGd@ICG-FA was observed at 36 h, which was prominently higher than that of GAM at 1 h (Figure S8c). This tumor maximum accumulation time point is consistent with NIR-II fluorescence imaging, validating the superior tumor targeting effect of our nanoprobe. To evaluate the biodistribution of VGd@ICG-FA in major organs, *ex vivo* NIR-II fluorescence imaging was also performed 36 h after injection (Figure 4e). The findings indicated that the fluorescent signal in the tumor site was predominantly concentrated, and fainter fluorescent intensity was discovered in reticuloendothelial system organs (liver and spleen), conclusively demonstrating the active recognition effect of VGd@ICG-FA to the tumor and notable ICG release under GSH stimuli.

NIR-II Fluorescent Imaging-Guided Tumor Resection in Microtumor-Bearing Mice Model and Residual Tumor Model. Encouraged by the aforementioned tumor-targeting capabilities of VGd@ICG-FA, we employed a microtumor mouse model to verify if the fluorescent nanoprobe could distinguish tiny tumors intraoperatively. We built tumors with volumes ranging from 1 to 10 mm^3 on the backs of mice by varying the concentration of 4T1-Luc cells injection. The bioluminescence signal and tumor fluorescence
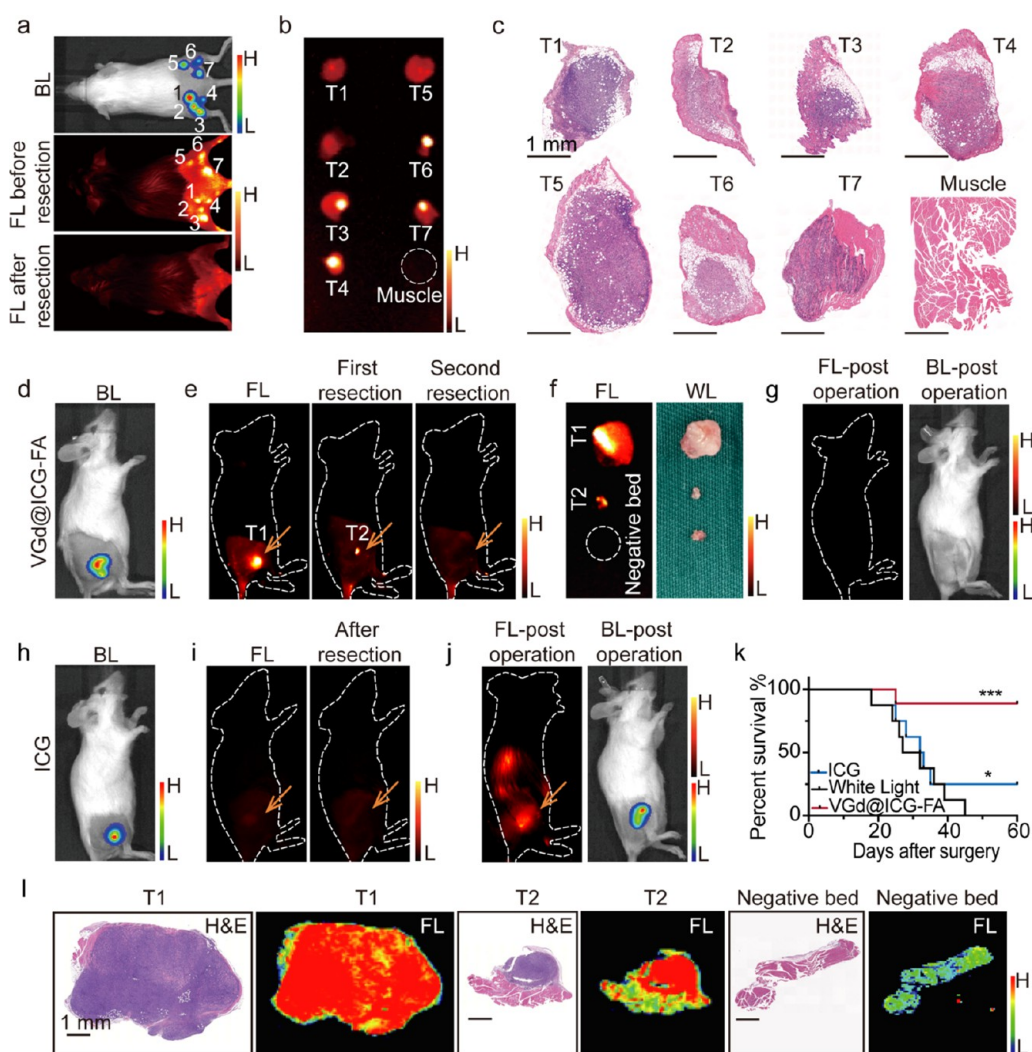
Figure 5. NIR-II fluorescent imaging-guided tumor resection in the microtumor-bearing mouse model and residual tumor model. (a) Presurgery bioluminescent image of 4T1-Luc microtumor-bearing mice before resection, and fluorescent images pre-NIR-II fluorescent imaging-guided surgery and after tumor resection. (b) NIR-II fluorescent images of resected tumor tissue and peritumoral muscle in the mice in a. (c) Corresponding H&E stained images in b. (d) Bioluminescent image of 4T1-Luc residual tumor model of the mouse in the VGd@ICG-FA group. (e) Fluorescent images presurgery and NIR-II fluorescent imaging-guided tumor resection images of mice in d. (f) Photograph and NIR-II fluorescent image of resected tumor tissue in the mice in e. (g) Fluorescence images postinjection of VGd@ICG-FA and bioluminescent image after 14 days postsurgery of mice in e. (h) Bioluminescent image of 4T1-Luc residual tumor model of the mouse in ICG group. (i) Fluorescent images presurgery and after-resection images of mice in h. (j) Fluorescence images postinjection of VGd@ICG-FA and bioluminescent image after 14 days postsurgery of mice in i. (k) Kaplan–Meier survival analysis of ICG, white light, and VGd@ICG-FA groups. (l) H&E staining analysis and NIR fluorescent images of 5 μm slices of f. The data are shown as the mean $\pm$ SD (*$p < 0.05$, **$p < 0.01$, ***$p < 0.001$, ****$p < 0.0001$).

signals were consistent (Figures 5a, b and S9), and tiny tumors were completely removed under NIR-II fluorescence imaging assistance. The pathological staining further confirmed seven distinct tumor boundaries (Figure 5c), suggesting that NIR-II fluorescence imaging-guided tumor surgery via VGd@ICG-FA had high dependability of intraoperatively outlining entire borders of small metastases.

Additionally, to assess the possibility of employing fluorescence image-guided surgery in accurately pinpointing any remaining malignancies, we built a 4T1-Luc residual tumor mouse model. First, tumor locations were evaluated by bioluminescence with an injection of D-luciferase potassium (Figure 5d, h). In the VGd@ICG-FA group, the nanoprobe-identified tumor profile had a high resolution and penetration depth compared to bioluminescence. After 36 h postinjection

of VGd@ICG-FA nanoprobe, the tumors were removed as entirely as possible under white light (T1, Figure 5e, f). Immediately afterward, the margin was observed under the NIR-II system to see if any signal remained. The residual tissue lightened up by the remaining NIR-II signal was removed thoroughly under fluorescence imaging (second fluorescent resection, T2, Figure 5e, f). Then, T1, T2, and muscle tissue from the negative bed were sliced for H&E staining. The H&E-stained images of dissected tissues clearly demonstrate the margins between the tumor and normal tissue, and no remaining tumors were observed in the muscle tissue. The fluorescence signal in tumor tissue was higher than that in para-tumor and normal tissue (Figure 5l), agreeing well with H&E staining. Simultaneously, 14 days after the surgery, no bioluminescence or NIR-II fluorescence was observed after the
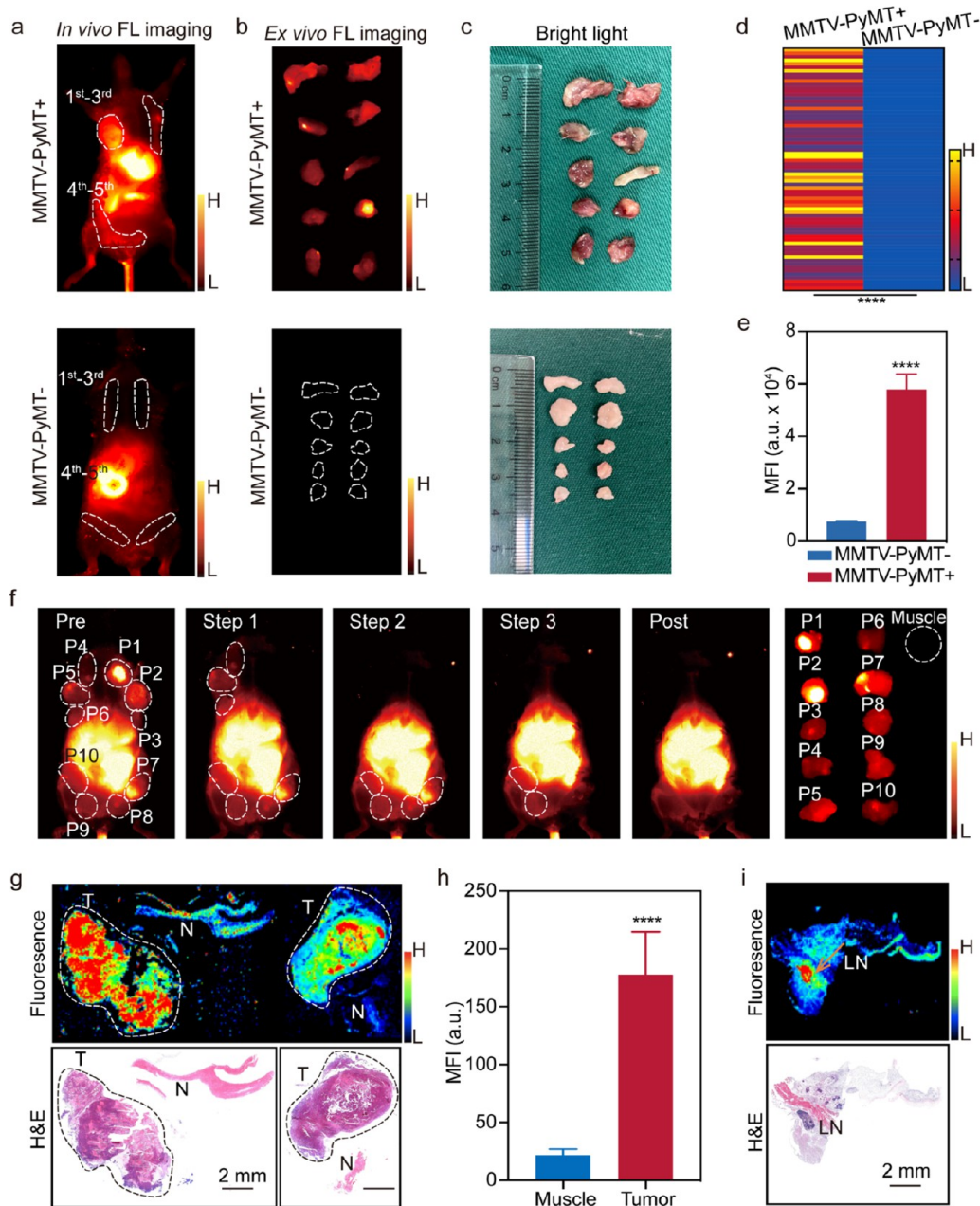
Figure 6. *In vivo* targeted fluorescent imaging and NIR-II fluorescent guided surgery after tail vein injection of VGd@ICG-FA in MMTV-PyMT mice model. (a) *In vivo* fluorescent images of MMTV-PyMT positive and negative mice. (b, c) *Ex vivo* fluorescent images and digital photographs of mammary glands of the mouse in a. (d) Mean fluorescent intensities of mammary glands tissue in MMTV-PyMT mouse. (e) The corresponding quantitative statistics of mean fluorescent intensity of MMTV-PyMT mouse. (f) NIR-II fluorescent imaging-guided surgery after intravenous injection of VGd@ICG-FA in a MMTV-PyMT positive mice model. From left to right: pre, 3 steps, postoperation, and resected tissue images. (g, i) NIR-II images and H&E staining analysis of resected tissue slices (5 μm) of PyMT positive mouse. (h) Corresponding mean fluorescence intensity of the resected tissue slices of f. The data are shown as the mean ± SD (*$p < 0.05$, **$p < 0.01$, ***$p < 0.001$, ****$p < 0.0001$).

injection of D-luciferase potassium and VGd@ICG-FA, representing the precise identification of the positive margin (Figure 5g). However, in the ICG group, only a weak fluorescence signal in the tumor site was found due to tumor targeting deficiency, highlighting an ICG utilization drawback in clinical surgery (Figure 5i). Similarly, in the ICG group, the tumor incision was carried out in white light first and no residual fluorescent signal was observed at the margin (Figure 5i). After 14 days, the recurrent tumor was clearly identified via NIR-II fluorescence image and bioluminescence image after

being injected with VGd@ICG-FA and D-luciferase potassium, respectively (Figure 5j). Finally, bioluminescence revealed a tumor recurrence rate of 75% (6/8) at 14 days in the ICG group and 87.5% (7/8) mice in the white light control group. By contrast, a recurrence rate was calculated as 12.5% in the VGd@ICG-FA group (Figure S10). Furthermore, VGd@ICG-FA was found to be efficacious in prolonging the survival rate (87.5%) during 60 days compared with the ICG group (25%) and white light group (12.5%) (Figure 5k). These results
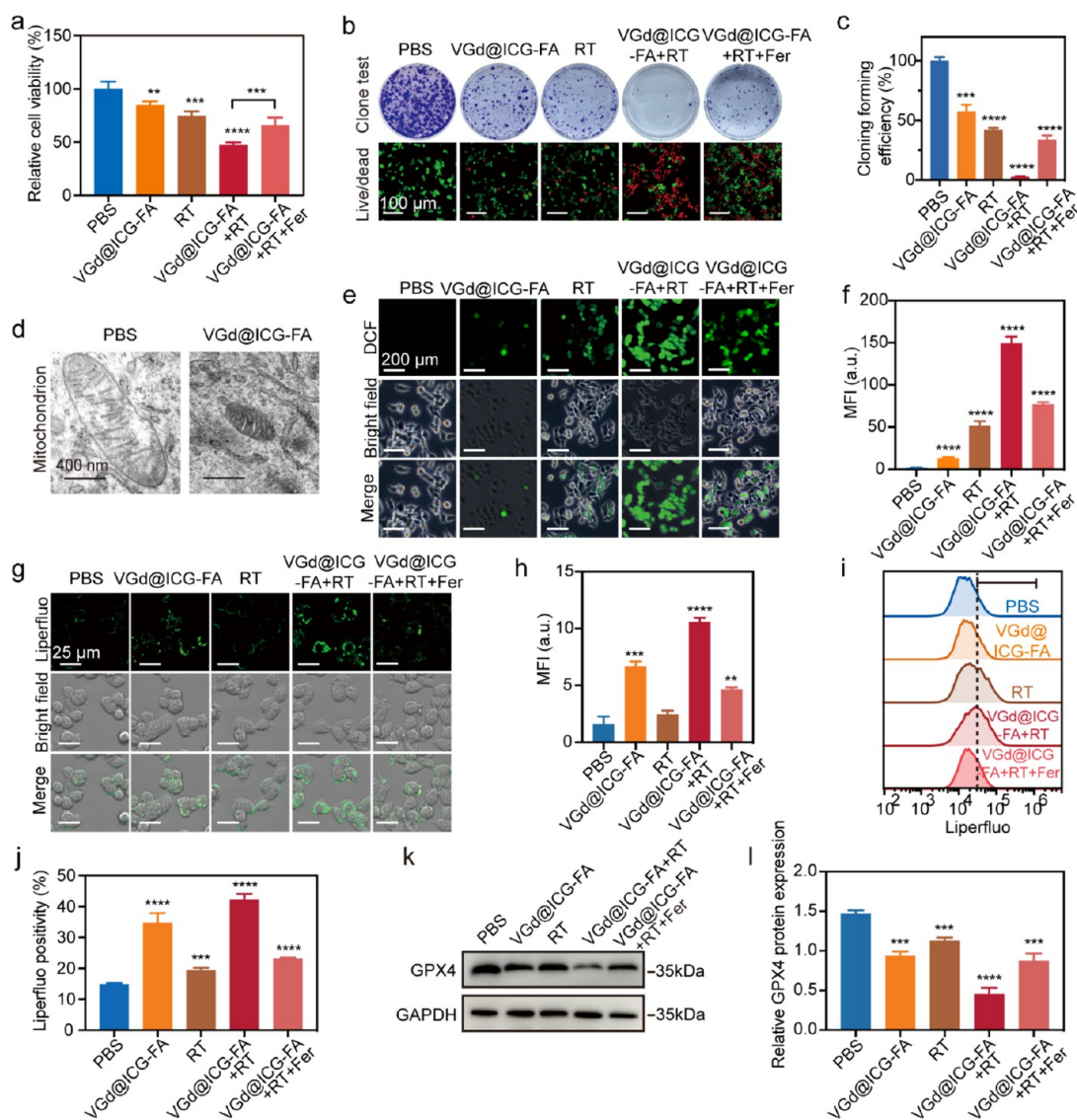
Figure 7. VGd@ICG-FA enhances radiotherapy sensitivity by ferroptosis through the GSH-ROS-LPO pathway *in vitro*. (a) Cell viability analysis of 4T1 cells after incubation with different formulations for 36 h. (b) Colony formation assays using 4T1 cells incubated with different formulations (above). CLSM images of live/dead assay using 4T1 cells (down). (c) The quantitative analysis of cloning forming efficacy in b. (d) TEM images of mitochondria in 4T1 tumor tissue after different treatments. (e) CLSM images of ROS in 4T1 cells after different treatments. (f) The quantitative analysis of mean fluorescence intensity in e. (g) CLSM images of Liperfluo in 4T1 cells after different treatments. (h) The quantitative analysis of mean fluorescence intensity in g. (i) Cytomembrane lipid ROS analysis after different treatments by flow cytometry. (j) The quantitative analysis of mean fluorescence intensity in i. (k) Western blot assays of the levels of GPX4 protein in 4T1 cells after VGd@ICG-FA inhibition and the level were reversed by Ferrostatin 1. (l) The quantitative analysis of mean fluorescence intensity in k. The data are shown as the mean ± SD (*$p < 0.05$, **$p < 0.01$, ***$p < 0.001$, ****$p < 0.0001$).

confirmed the efficacy of the nanoprobe for complete tumor dissection under NIR-II fluorescence imaging.

NIR-II Fluorescence Targeted Imaging-Guided Surgery in Spontaneous Breast Cancer Mouse Model. Based on our success in the subcutaneous 4T1-bearing tumor model above, the MMTV-PyMT mouse model was chosen to depict spontaneous breast tumor development in humans to further validate the targeting property of our nanoprobes.[49] After intravenous injection of VGd@ICG-FA for 36 h, MMTV-PyMT+ mice showed substantially greater mammary gland fluorescence signals both *in vivo* and *ex vivo* than MMTV-PyMT− mice with healthy breast tissue (Figures 6a, b, c, and S11). Fluorescence intensity quantitative analysis showed that the VGd@ICG-FA in mammary tumors was 7.59 times higher than in normal tissues, which was high enough to significantly

distinguish tumors from normal mammary tissue (Figure 6d, e). Similarly, we conducted surgical navigation in the MMTV-PyMT+ mouse model. After the tail vein injection of VGd@ICG-FA for 36 h, 5 pairs of mammary tumors were excised in segments under NIR-II fluorescent imaging navigation (Figure 6f). The mean fluorescence intensity of resected tumors was much higher than that of the adjacent muscle tissue with a tumor/muscle (T/M) ratio of 8.01 ± 0.62 (Figure S12). The tumor sections then underwent H&E staining and NIR-I microscopic fluorescence imaging analysis. The microscopic fluorescence intensity distinctly differentiated between cancer tissues and nearby muscle tissues, and they coincided with the outputs of the H&E staining results (Figure 6g), indicating the nanoprobe could accurately identify tumor margins. The T/M ratio was up to 8.14 ± 0.51 (Figure 6h), which showed good
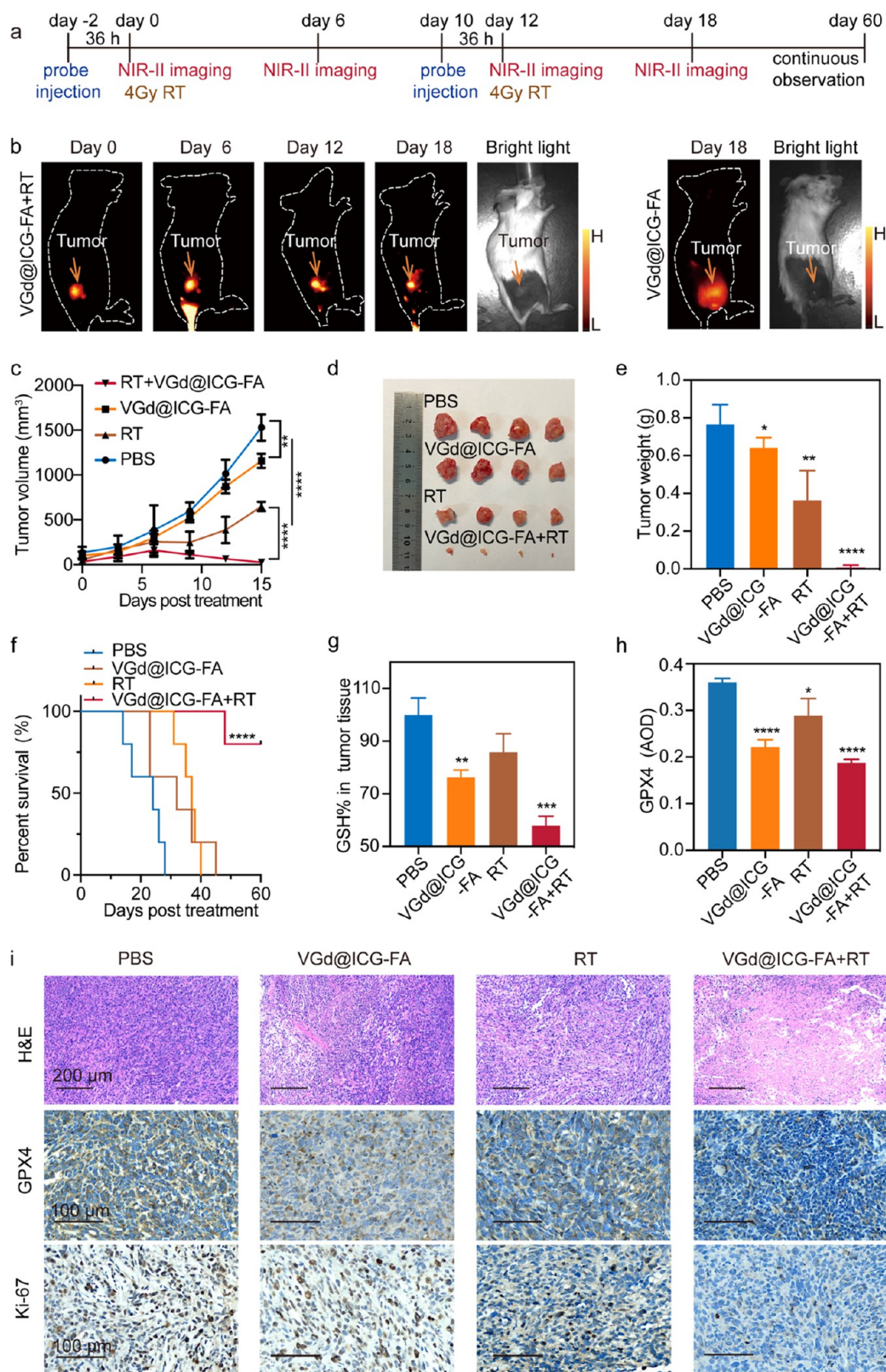
Figure 8. *In vivo* precise radiotherapy evaluation and enhanced radiotherapy sensitization by ferroptosis. (a) Schematic illustration of radiotherapy enhanced by ferroptosis in 4T1-Luc bearing mice with NIR-II fluorescent imaging guidance. (b) *In vivo* NIR-II fluorescent images of mice in the VGd@ICG-FA+RT group (left) or VGd@ICG-FA group (right) from day 0 to 18 and bright light image at day 18. (c) Time-dependent tumor growth curves after various treatments. (d) Photograph of tumors after the various treatments on day 15. (e) Tumor weights of mice on day 15 after different treatments. (f) Survival curves of the mice with different treatments. (g) GSH concentrations in tumor tissue after various treatments. (h) Average optical density analysis of GPX4-stained images of mice after various treatments of 15 days. (i) H&E and immunohistochemistry analysis of GPX4 and Ki67 from different groups of mice at 15 days of treatments. The data are shown as the mean $\pm$ SD (*$p < 0.05$, **$p < 0.01$, ***$p < 0.001$, ****$p < 0.0001$).

agreement at the tissue level in Figures 6e and S12. Surprisingly, the lymph nodes displayed relatively higher fluorescence intensity, leading to the potential of guiding sentinel lymph node biopsies via our fabricated NIR-II nanoprobes (Figure 6i) and this was worth further exploration. Generally speaking, the above different tumor models indisputably demonstrated high dependability in NIR-II fluorescence imaging-guided tumor surgery.

VGd@ICG-FA Enhanced Radiosensitivity *In Vitro* by Inducing Ferroptosis through the GSH-ROS-LPO Pathway. BCS is the recommended route of therapy for early breast cancer, while for patients with advanced breast cancer, RT is a crucial palliative option.[50] As our nanoprobe enables to promote the production of ROS, we speculate if it could promote radiotherapy efficacy. Thus, we investigated the efficiency of VGd@ICG-FA for the radiosensity of 4T1 cells. VGd@ICG-FA incubated with 4T1 tumor cells caused a reduction in cell viability after X-ray irradiation (47%) compared to the single radiation (74%) and the VGd@ICG-FA group (84%) (Figure 7a). In addition, similar decrease trends in colony formation assay and live/dead staining images were found (Figure 7b). Interestingly, VGd@ICG-FA combined RT treatment decreased colony formation sharply to 2.5% (Figure 7c). Accordingly, we compared the effect of radiotherapy sensitization by γH_2AX immunofluorescence analysis[51] to see the extent of DNA double-strand breaks. We found that the DNA damage level of VGd@ICG-FA combined RT treatment was significantly higher than that of the RT group, further confirming the exceptional radio-sensitization enhancement of our Gd-based nanoprobes under X-ray irradiation (Figure S13). In conclusion, the above results confirmed the probe's crucial effect on radiotherapy sensitization.

Previous experiments verified that our probe disrupted intracellular redox homeostasis and reduced GSH levels. Therefore, we speculated that the probe could trigger ferroptosis and that the Gd-induced massive production of ROS during radiotherapy could further enhance ferroptosis, which may finally induce potent radiotherapy sensitization. We further explored the mechanisms underlying nanoprobe-induced ferroptosis. The cytotoxicity decreased from 66% to 47% ($p < 0.0001$) after adding the ferroptosis inhibitor, Ferrostatin 1 (Fer) (Figure 7a). And Fer reversed the cloning forming rate from 2.5% to 34%, further confirming the crucial effect of ferroptosis during radiotherapy sensitization (Figure 7c). Significantly, the mitochondria in tumor cells were shrunken with increased membrane density in the VGd@ICG-FA group (Figure 7d), which had been regarded as characteristic of ferroptosis.[52,53]

Moreover, GSH, as an antioxidant, was crucial in reducing LPO generated by eliminating intracellular ROS.[54] Inspired by the GSH depletion of VGd@ICG-FA in Figure 3c, the alterations of ROS and LPO were explored to convince the ferroptosis in radiosensitization. Intracellular ROS was detected by 2,7-dichloro-fluorescin diacetate (DCFH-DA), which can be oxidized by intracellular ROS to highly emissive DCF with green fluorescence. Comparative cell killing efficacy, living cell numbers and intracellular ROS accumulation were found in VSN@ICG-FA and VGd@ICG-FA groups (Figure S14a, b). Interestingly, both nanoprobes treated cells showed some extent of green fluorescence intensity, verifying that the ROS generation was mediated by the GSH depletion in the cytoplasm (Figures 7e, f and S14c). When combined with RT,

the VGd@ICG-FA treated cells exhibited much higher green fluorescence intensity compared with the other groups (Figure 7e, f). The above results indicated that the Gd component was vital in successfully inducing the most efficient ROS accumulation when exposed to X-ray, while after adding Fer, the fluorescence intensity decreased to nearly half, indicating that Fer successfully cleared the ROS in the cell (Figure 7e, f).

Another characteristic of ferroptosis is the buildup of LPO.[39] Liperfluo-stained analysis revealed that the LPO levels in VGd@ICG-FA treated group were two folds higher after RT, whereas Fer attenuated LPO production down to one-third (Figure 7g, h). Quantitative analysis using flow cytometry showed similar results: increased LPO positive cells in VGd@ICG-FA were enhanced after RT treatment and this increasing trend drops to nearly half by Fer meditation (Figure 7i, j). As reported, the GSH-dependent lipid peroxidase GPX4 prevented ferroptosis, therefore GPX4 reflected the variation of ferroptosis.[39] Western blot assay showed that the VGd@ICG-FA incubation group upon RT exhibited an obvious reduction of GPX4 compared to the group without RT. The reduction of GPX4 was reversed by Fer (Figure 7k, l). Hence, the above results confirmed that VGd@ICG-FA activated radiosensitivity *in vitro* by inducing ferroptosis through the GSH-ROS-LPO pathway.

VGd@ICG-FA Guided Radiotherapy and Enhanced Radiosensitivity through Ferroptosis *In Vivo*. Next, we sought to evaluate the radiosensitivity efficacy of VGd@ICG-FA combined with RT *in vivo*. Figure 8a showed the diagram of the tumor therapy procedure treated with VGd@ICG-FA and RT. By the NIR-II fluorescent imaging system, the probe was capable of observing the specific accumulation in the tumor and clearly monitoring the size and tumor elimination efficiency (Figure 8b). This result verified the utilization of VGd@ICG-FA in the target delineation of radiotherapy and continuous monitoring of tumor size changes during radiotherapy. The VGd@ICG-FA treated mice exhibited slight tumor growth inhibition that could be ascribed to ferroptosis. Prominently, combined with RT, VGd@ICG-FA treated mice present the most efficient tumor regression compared to other groups (Figure 8c). Similarly, the tumor weights of the VGd@ICG-FA combined RT group also demonstrated the optimal antitumor efficiency (Figure 8d, e). These results further suggested the tumor cell elimination effect of ferroptosis combined with RT. With regard to the overall survival rate, the *in vivo* results demonstrated that nanoprobe improves the overall survival rate of mice, especially with RT (Figure 8f). In brief, the tumor suppression ability of the VGd@ICG-FA combined RT treatment reflected the great potential in radiotherapy sensitization.

To further evaluate the effect of ferroptosis, GSH levels in the tumor tissue were detected. In both VGd@ICG-FA alone and VGd@ICG-FA combined RT groups, GSH concentration declined to 76.2% and 57.8%, respectively. While in the RT group, it only slightly decreased to 87.8% (Figure 8g). Then, the mouse tumor tissues were collected for H&E and immunohistochemistry staining. H&E results revealed that tumors in the VGd@ICG-FA combined RT group undergo significant necrosis, large nuclear fragmentation, and nuclear shrinkage, showing the RT sensitization efficacy of VGd@ICG-FA (Figure 8i). Strikingly, compared to other groups, GPX4 decreased significantly in VGd@ICG-FA combined RT groups, verifying the successful inducement of ferroptosis (Figure 8h, i). Besides, compared with the untreated group,

Ki67-positive cells were lower in the treated groups: 5.5% in the VGd@ICG-FA + RT group, 26.4% in the RT group, 38.2% in the VGd@ICG-FA group, and 44.6% in the PBS group (Figure S15). The significant decrease of Ki67 suggested that the VGd@ICG-FA effectively inhibited the proliferation of tumors with radiation. These data indicated that ferroptosis induced by VGd@ICG-FA had a promising effect on the sensitization of RT, especially in advanced breast cancer.

Biosafety Evaluation of VGd@ICG-FA *In Vivo*. Inspired by the fascinating surgical applications and RT sensitivity effects, biosafety was evaluated to assess the potential for further clinical translations. No significant weight losses were observed in all mice during the treatment, indicating no severe burden caused by the tumors and probes (Figure S16). Blood indices and serum biochemical indicators were all at normal levels within 28 days (Figure S17). These findings suggested that our nanoprobes did not significantly harm the body. To evaluate the toxicity of VGd@ICG-FA on the GSH-rich organ, the liver, different doses of VGd@ICG-FA were injected and a negligible fluctuation in the levels of hepatic microsomal proteins was detected, thereby giving clear evidence of safety concerns (Figure S18). Lately, this harmless quality had been validated by collagen deposition and skin morphology, which showed no significant differences within 28 days compared to the PBS injected group (Figure S19). The pathological studies of the major organs (heart, liver, spleen, lung, and kidney) from the normal BALB/c mice injected with VGd@ICG-FA illustrated a nontoxic quality at the dose of 32 μg/mL (Figure S20). These results confirmed the high biocompatibility of VGd@ICG-FA, which provided great potential biosafety assurance for future clinical applications of VGd@ICG-FA.

DISCUSSION

BCS is a well-accepted standard of care for patients with early stage breast cancer. Precise margin assessment during the operation can reduce re-excision rates and debate is ongoing regarding how to evaluate resection margins to ensure the radical removal of all cancer cells.[55] Pathological examination is regarded as a gold standard for evaluating tumor margin, but it is time-consuming and has discrepancies.[56] Although researchers have developed several ways to evaluate the surgical margin, such as 3D specimen X-ray imaging and CT reconstruction,[57] these imaging methods are challenging to delineate normal from tumor tissue in real time, high sensitivity, and specificity methods.

We have always been exploring strategies to visualize the tumor margins when conducting BCS. Human Serum Albumin-ICG (HSA-ICG) was applied to guide surgical resection, and the signal on the surgical bed could be used to guide surgery while the tumor-to-noise ratio was low (approximately 2.5).[58] On the other hand, R&HV−Gd allowed complete tumor excision under NIR-II fluorescent imaging guiding by reducing aqueous instability and improving target specificity of ICG, but the biosafety of rare-earth-based nanoprobes merited attention.[21] Most recently, our group developed a self-assembled multifunctional nanoprobe ^Gd^DTPA-HSA@ICG-Bevacizumab to improve the efficacy of NIR-II fluorescence image-guided breast cancer surgery, but the photobleaching of ICG is a hurdle to overcome.[59]

Taking the advantages of less tissue scattering and nonradiative effect, NIR-II imaging can provide delicate anatomical structures and have a great advantage in dynamically displaying tumor boundaries in real-time.[60]

Among the clinical fluorophores currently approved by the FDA, only ICG has the ability to fluoresce in the NIR-II region. However, its application is limited due to its instability and nontargeting characteristics. For example, when used in clinical surgery, aqueous ICG solution begins to degrade within 5 min of exposure to the operating table light and undergoes significant degradation at 110 min.[13,43] In this study, we have greatly improved the stability of aqueous ICG to 96 h. Moreover, our nanoprobe effectively enhances its resistance to photobleaching by encapsulating ICG inside spherical particles, maintaining nearly 98% fluorescence intensity with up to 30 min of laser irradiation, and providing stable images for long-term surgery. Because of nontargeting characteristics, ICG is rapidly metabolized and cannot effectively aggregate in the tumor. Here, by loading in VGd@ICG-FA, ICG is able to specifically target tumor tissue and quickly enter tumor cells with the advantage of virus-like morphology. By comparing the targeting experiments, we can see that the anchoring of FA brings about a superior aggregation of the probe and increases the TBR from 5 to 8. The substantial improvement in ICG-specific targeting brought about by VGd@ICG-FA provides the basis for a broader application of ICG.

It was reported that breast carcinomas were unifocal in 36%, multifocal in 35%, and diffuse in 28% of patients.[61] Finding satellite lesions, especially some tiny cancers, is extremely difficult. Our probe is expected to illuminate tiny satellite lesions and guide precise and adequate resection with its property of identifying 1 mm³ tiny tumors. Therefore, the clear outline of tumor boundaries, the identification of tiny tumors, and stable illumination brought by VGd@ICG-FA provide a platform for precise surgery.

Radiotherapy is a crucial treatment that raises the local control rate and improves survival over the long-term. It has been frequently used on patients with advanced breast cancer or those with early stage breast cancer who received breast-conserving surgery.[62,63] Precise radiotherapy enables radiation to be delivered to the target lesions and spares nearby normal tissues. Our probe can pinpoint the tumor location by the NIR-II imaging system and monitor the change of the tumor boundary during radiotherapy by fluorescence.

Radiation resistance remains another major challenge, resulting in RT failure, cancer relapses, and distant metastasis. Our GSH-depleted and Gd-coating probe can boost the efficacy of RT. When VGd@ICG-FA is used alone, it can activate ferroptosis by depletion of GSH, causing inactivation of the GSH catalase GPX4, which allows large amounts of LPO to accumulate. When combined with radiotherapy, Gd, a high atomic number element, can produce a large amount of ROS which can further generate LPO accumulation and enhance ferroptosis to achieve radio sensitization.[64] Compared with traditional radiation sensitizers like cisplatin or fluorouracil or recently developed radio-sensitizer, VGd@ICG-FA has tumor-targeting specificity and mainly agglomerates in tumors, therefore reducing systemic toxicity. So, this nanoprobe may be used for palliative radiotherapy in inoperable locally advanced or metastatic breast cancer to improve the efficacy of RT. Undeniably, by comparison with VSN@ICG-FA+RT, it was a certain significant improvement (10%) of cell killing in VGd@ICG-FA+RT, while the large majority of RT-induced cell toxicity is not sensitized by Gd. Although our constructed probes have excellent fluorescence imaging and therapeutic effects, the construction procedure of our Gd-based nanoprobe

is quite complicated, mainly including VGd fabrication, ICG loading, and FA modification. Indisputably, each step of purification is troublesome, therefore it is impossible to optimize all components. In addition, the long-term toxicity, in-depth effects on metabolism, as well as the fate of nanoprobes remain to be investigated. Further inspection studies examining the systemic and breast cancer delivery of nanoprobes in large primates are needed.

CONCLUSIONS

In summary, we have developed a multifunctional nanoprobe for NIR-II fluorescence imaging-guided precise breast cancer surgery and radio-sensitization induced by ferroptosis via VGd@ICG-FA. The prepared probe VGd@ICG-FA significantly improves TBR in the NIR-II fluorescence imaging owing to the virus-like morphology and FA anchoring. Pathological data from various tumor models indicate that our probes can successfully distinguish tumor tissues from normal tissues and achieve negative surgical margins. Furthermore, the probe can be used to precisely delineate the target tumor location and therapeutic efficiency during the treatment with NIR-II fluorescence imaging. The induced ferroptosis by the GSH-ROS-LPO pathway enhanced a strong radio-sensitization. More encouragingly, this nanoprobe is free of organ damage and acute harm, thereby offering the potential for future clinical translation.

MATERIALS AND METHODS

Materials. Hexadecyltrimethylammonium bromide (CTAB), tetraethyl orthosilicate (TEOS), Bis[3-(triethoxysilyl)propyl]tetrasulfide (BTES), and (3-aminopropyl)triethoxisilane (APTES) were purchased from Sigma-Aldrich Company (St Louis, MO, USA). Gadolinium chloride hexahydrate ($GdCl_3 \cdot 6H_2O$), cyclohexane, hexamethylenetetramine, N-hydroxysuccinimide (NHS), N-(3-(dimethylamino)propyl)-N'-ethylcarbodiimide hydrochloride (EDC), and potassium ferrocyanide were bought from Aladdin Reagent Co. Ltd. (Shanghai, China). FA-PEG-COOH was purchased from Ponsure Biological (Shanghai, China). Indocyanine green (ICG) was purchased from Sangon Biotech (Shanghai, China). D-Luciferin potassium salt was from Beyotime (Shanghai, China). RPMI 1640 medium and fetal bovine serum (FBS) were purchased from Gibco Life Technologies (New York, NY, USA). MEBM medium was purchased from Lonza (Basel, Switzerland).

Synthesis of VGd@ICG-FA. Synthesis of VSN and VGd: CTAB (0.75 g) was dissolved in 60 mL water and 1 mL 0.1 M of NaOH was added. Then the mixture was put into an oil bath and stirred for 30 min at 60 °C. Soon afterward, cyclohexane containing 3.56 mL TEOS and 0.44 mL BTES was slowly added dropwise. After 72 h of reaction, VSN was obtained by centrifugation and then rinsed with water and ethanol. Next, VSN was dispersed in 60 mL water. VGd was prepared by mixing VSN and hexamethylenetetramine (50 mg) for 4 h at 90 °C for 30 min, and then $GdCl_3 \cdot 6H_2O$ (50 mg) was added. VGd can be obtained after 30 min stirring.

Synthesis of VSN (nontetrasulfide doping): CTAB (0.75 g) was dissolved in 60 mL water and 1 mL 0.1 M of NaOH was added. Then the mixture was stirred for 30 min at 60 °C. Afterward, cyclohexane containing 4 mL TEOS was slowly added dropwise. After 72 h of reaction, VSN was obtained.

Amino group modification on VGd: Following a dropwise addition of 200 μL APTES, VGd in ethanol was stirred at 75 °C for 12 h. The solid VGd-NH$_2$ was obtained by washing it with ethanol and water 3 times.

Synthesis of VGd@ICG-FA: Add 5 mL of 2 mg/mL VGd-NH$_2$ to 1 mL of 1 mg/mL ICG and stir together overnight. After 10 min centrifugation (10000 rpm) of the sample, VGd-NH$_2$@ICG was obtained. Then 3 mg of FA-PEG-COOH, 2 mg of EDC, and 1 mg of

NHS were added into 15 mL of 2 mg/mL VGd-NH$_2$@ICG aqueous solution. After stirring for 48 h at room temperature, the sample underwent rinsing three times to get rid of uncombined ICG and FA-PEG-COOH. Finally, the VGd@ICG-FA nanoprobes were dissolved in diluted water and stored at 4 °C in the dark.

Characterization of VGd@ICG-FA. The morphology and dimensions of the nanoprobes were explored using transmission electron microscopy (TEM, H-7650, Hitachi, Japan) and scanning electron microscopy (SEM, S-4800, Hitachi, Japan). Elemental analysis was performed using high-resolution transmission electron microscopy (HRTEM, FEI Tecnai F20, accelerating voltage = 200 kV). A Fourier infrared spectrometer (FT-IR, Nicolet iS 50, Thermo Fisher, USA) was used to detect the surface groups of particles. UV−vis spectra were measured by a UV−vis−NIR spectrophotometer (Cary 5000, Agilent, USA). Dynamic light scattering (DLS, Omni, Brookhaven, USA) was utilized to determine the hydrodynamic diameter distribution, polydispersity, and zeta potential of the probes.

ICG and VGd@ICG-FA Photostabilities. ICG and VGd@ICG-FA were continuously irradiated by an 808 nm laser for 30 min in a 96-well plate. Additionally, samples were kept at 25 °C in the dark for 96 h in order to assess the stability of ICG and VGd@ICG-FA in aqueous solutions. UV−NIR absorption spectra were measured at different time points.

Protein Expression Analysis and VGd@ICG-FA Cytotoxicity. The human normal mammary epithelial cells MCF-10A, human breast cancer cell MCF-7, MDA-MB-231, BT549, and mouse breast cancer 4T1 cell lines were purchased from the American Type Culture Collection (Rockville, USA). In an incubator, MCF-10A cells were grown in MEBM medium, MCF-7, and MDA-MB-231 cells were grown in DMEM medium, and BT549 and 4T1 cells were grown in RPMI 1640 medium. All the mediums contained 10% FBS and 1% penicillin−streptomycin.

As for protein expression analysis, Western blot was performed as previously described[65] with a specific primary antibody: rabbit monoclonal antibody to FOLR1 (ab221543, abcam), GPX4 (ab125066, abcam), or GAPDH(ab181602, abcam) diluted 1:1000 overnight at 4 °C and HRP-labeled goat antirabbit antibody (#7074, cell signaling technology) or goat antimouse antibody (#7076, cell signaling technology) at room temperature for 1 h.

The level of FOLR1 mRNA expression was examined using qRT-PCR. The primers used were: FOLR1 Forward: CTGGCT-GGTGTTGGTAGAACAG, FOLR1 reverse AGGCCCCGAGGA-CAAGTT, GAPDH Forward: 5′-GGCAAATTCCATGGCACCGT-3′, GAPDH reverse: 5′-TGGACTCCACGACGTACTCA-3′.

Cell Viability Studies. In 96-well plates, 5×10^3 MCF-10A and 4T1 cells were planted in each well before being cultured for an additional overnight. After that, the fresh medium containing a series concentration (0−256 μg/mL) of VGd@ICG-FA was used to incubate cells for 36 h, and then cell viability was measured by the CCK-8 cell-counting kit (Beyotime, Shanghai, China). Further, to evaluate the cytotoxicity of VGd@ICG-FA combined with RT, 4T1 cells were incubated with VGd@ICG-FA for 36 h followed by irradiation of 4 Gy X-rays.

GSH-Triggered Degradation and GSH-Exhausting Detection. VGd@ICG-FA was dissolved in PBS or 10 mM GSH with a final concentration of 100 μg/mL at different points of time. The solutions were shaken continuously at 37 °C and studied under TEM at distinct times. In addition, 4T1 cells were incubated with the medium containing different doses (0−128 μg/mL) of VGd@ICG-FA. After that, GSH concentration was determined by the Micro Reduced GSH Assay Kit (Solarbio, Beijing, China). Likely, after intravenous injection of the probe and treatment with or without RT, the tumor tissue was resected and ground into homogenate to measure the GSH content with the same kit.

Cellular Uptake of VGd@ICG-FA. To verify whether the virus-like nanoparticles would be more rapidly taken up by 4T1 cells, we synthesized a smooth mesoporous silica nanoparticle as the control in the following steps. First, 1.5 mg of CTAB was dispersed in 60 mL water and the mixture was stirred at 60 °C. Then 0.72 mL of 25% triethanolamine was added to the solution. Twenty milliliters of a

mixture of cyclohexane (16 mL) and TEOS (4 mL) was dropped onto the water layer. After 48 h, the smooth mesoporous silica nanoparticles were obtained after centrifugation at 10,000 rpm for 10 min. Finally, this nanoparticle was loaded with ICG. 1.5×10^5 4T1 cells were incubated with VGd@ICG, MSN@ICG, or VGd@ICG-FA at equivalent 3 μg/mL ICG concentrations in six-well plates or on glass slides. The cells incubated in plates were measured by a flow cytometer (CytoFlex). The cells incubated on glass slides were fixed with 4% paraformaldehyde and stained with DAPI for fluorescence microscopy assessment.

***In Vivo* Targeted Imaging, Biodistribution, and Block Imaging.** Six-week-old female BALB/c mice were purchased from Gempharmatech Co., Ltd. (Jiangsu, China) and bred in Xiamen University Laboratory Animal Center. All animal experiments obtained acceptance from the animal procedures approved by the Institutional Animal Care and Use Committee of Xiamen University. All studies were carried out in strict accordance with the relevant guidelines.

Each BALB/c mouse was subcutaneously injected with 50 μL PBS containing 1×10^7 4T1-Luc cells at the right hind limb. The formula "width^2 × length × 0.5" was used to determine the tumor volume. When their size was about 200−300 mm^3, they were randomly injected with VGd@ICG-FA, VGd@ICG, or free ICG at an equivalent ICG concentration (1 mg/kg) (n = 3). At different time points, the fluorescence signal was evaluated using a NIR-II fluorescence imaging system (III series 900/1700, Suzhou Yingrui Optical Technology Co., Ltd.). As for the *in vivo* MRI analysis, mice were injected with VGd@ICG-FA or gadoteric acid meglumine (GAM) containing the same concentration of $[Gd^{3+}] = 25 \times 10^{-6}$ M/kg. MRI was conducted by 9.4 T BioSpec MRI (Bruker, Germany), and T1-weighted images were obtained with parameters as follows: TR = 1000 ms, TE = 8.5 ms, FOV = 4 × 4, slices = 20.

In vivo biodistribution of VGd@ICG-FA was also observed. 4T1-Luc tumor-bearing mice were injected with VGd@ICG-FA and then tumor, major organs, and muscle tissues (i.e., heart, liver, spleen, lung, and kidney) were isolated at 36 h and underwent NIR-II fluorescence imaging.

In the blocking experiments, FA (100 μg) was administered intravenously to mice 10 min ahead, and then the NIR-II fluorescence signal was collected.

Microtumor Identification. 5−20 μL PBS containing 5×10^6 4T1−Luc cells were subcutaneously injected to BALB/c mice at various places in the back. The location of microtumors was verified by IVIS bioluminescent imaging system (PerkinElmer, Waltham, Massachusetts, USA). Afterward, at 36 h postinjection of VGd@ICG-FA ($[ICG]$ = 1 mg/kg), tumors were excised under NIR-II fluorescent real-time imaging guidance (exposure time 150 ms, excitation power density 0.1 W/cm^2). All removed tissues including paracancerous tissues proceeded for histological examination.

NIR-II Fluorescence-Guided Real-Time Tumor Surgery. 4T1-Luc tumor cells were implanted near the right leg of the mouse and ensured that the tumor could infiltrate and grow into the muscle at a later stage. We used bioluminescence to confirm the presence of the tumor and roughly estimate the location. Surgical resection was performed by visualization and palpation under white light just like the clinical surgery. In the VGd@ICG-FA group and the VGd@ICG group, the mice were reimaged by the NIR-II fluorescence imaging system. If there was a residual fluorescent signal in the tumor surgical bed, further resection was performed until no signal was present. The paracancerous muscle tissue was also excised as a control. Fourteen days after surgery, all mice performed bioluminescent imaging to observe recurrence. Then, the tissues were taken for histological investigation and NIR fluorescence analysis (Odyssey CLx, LI-COR Biosciences, Nebraska, USA) by fluorescence flatbed scanning.

Transgenic MMTV-PyMT positive and negative mice (FVB/N-Tg (MMTV-PyMT) 634 Mul/J) were purchased from the Jackson Laboratory (Bar Harbor, ME, USA). 36 h after VGd@ICG-FA injection, the NIR-II fluorescence imaging was obtained. In the surgical model of transgenic mice, each abnormally luminous mammary gland of positive mice was gradually excised under NIR-

II fluorescence guidance. Finally, muscle tissue was excised as a control.

Analysis of Radio Sensitization Induced by Ferroptosis *In Vitro*. 1×10^5 4T1 cells were seeded in a CLSM culture vessel, and they were then treated with VGd@ICG-FA for 36 h. For cell ROS detection, after the coincubation with DCFH-DA (10 μM, Beyotime) for 20 min, the cells received X-ray irradiation (4 Gy). Subsequently, the cells were imaged by CLSM. In the group containing Ferrostatin 1 (Fer, HY-100579, MCE) treatment, 5 μM Fer was added into the medium together with VGd@ICG-FA.

For lipid peroxidation analysis, 1×10^5 4T1 cells were incubated with VGd@ICG-FA for 36 h. Cells received the X-ray irradiation (4 Gy) and then were incubated for 30 min with liperfluo (1 μM, L248, Donjindo). Besides, lipid peroxidation levels were also evaluated by flow cytometry. For live/dead analysis, a Calcein/PI staining assay (C2015L, Beyotime) was used to detect cell survival via CLSM. For γH_2AX analysis, a DNA Damage Assay Kit (C2035S, Beyotime) was used and the cells were detected via CLSM.

Ferroptosis Enhanced RT Sensitization Analysis *In Vivo*. BALB/c female mice with subcutaneous 4T1 tumors (20−30 mm^3) were divided into four groups: (1) PBS, (2) VGd@ICG-FA, (3) RT only, and (4) VGd@ICG-FA + RT. Mice in groups (1), (2), and (4) received 50 μL VGd@ICG-FA ($[ICG]$ = 1 mg/kg) or 50 μL PBS by tail vein injection on days −2 and 10 of treatment, and then groups (3) and (4) received a single dose of X-rays (radiation dose = 4 Gy) on days 0 and 12. Tumor size was recorded and weighed every 3 days. After 15 days of treatment, some mice in each group were randomly sacrificed and tumor sections as well as major body organs were collected for H&E and IHC staining, including GPX4 (ab125066, abcam), and Ki67 (ab15580, abcam). The remaining mice were observed continually until 60 days post-treatment.

Tissue TEM Imaging. To confirm the ferroptosis in the tumor, 4T1-bearing mice with 100−200 mm^3 tumors were injected with PBS or VGd@ICG-FA. After 3 days, tumor tissues were collected, fixed, and dehydrated. Then the tissue was stained by heavy metal electrons and observed by TEM.

***In Vivo* Biosafety Studies.** To assess *in vivo* biosafety, liver microsomal proteins were assayed using the bicinchoninic acid method. After being injected with different concentrations of VGd@ICG-FA for 7 days, liver tissues were removed and rinsed with KCl solution (0.15 M), and liver microsomal proteins were obtained by multiple centrifugations of tissue homogenates. In detail, the supernatant was collected after the centrifugation at 300g, 700g, 2200g, and 700g, each time for 30 min at 4 °C. After the last centrifugation, the BCA kit (PC0020, Solarbio) was used to measure the protein concentration. In addition, we performed H&E staining of the major organs at the end of the treatment. At 1, 3, 7, and 28 days, blood samples were collected for electrolyte, blood biochemical, and hematological tests. In addition, to assess the skin and muscle infiltration toxicity of VGd@ICG-FA, Masson staining of skin and muscle was performed.

Statistical Analyses. Data were obtained from at least three independent measurements ($n \geq 3$) to ensure the reproducibility of the experiment. Means were compared using a two-tailed Student's t test or one-way ANOVA. The survival benefit was determined using Kaplan−Meier analysis (Graph Pad Prism). In all types of statistical analysis, $P < 0.05$ were considered significant.

ASSOCIATED CONTENT

Ⓢ Supporting Information

The Supporting Information is available free of charge at https://pubs.acs.org/doi/10.1021/acsnano.3c00350.

> Additional results for nanoparticle SEM results, EDS analysis, ICG calibration, nanoparticles' photographs, FT-IR spectra, the UV−vis−NIR absorption spectra, ICG and Gd release analysis, TEM images and cell viability analysis of VGd@ICG-FA-, MRI images, figures of bioluminescent images, fluorescent images, mean

fluorescence intensity, γH_2AX immunofluorescence analysis, Gd-induced cell viability, live/dead analysis, CLSM images of ROS, Ki67 percentage, body weight changes, hematology analysis, microsomal protein analysis, Masson staining analysis, and H&E staining analysis (PDF)

AUTHOR INFORMATION

Corresponding Authors

Peiyuan Wang − *Key Laboratory of Design and Assembly of Functional Nanostructures, Fujian Institute of Research on the Structure of Matter, Chinese Academy of Sciences, Fuzhou 350002, China;* ⓘ orcid.org/0000-0003-1700-1061; Email: wangpeiyuan@fjirsm.ac.cn

Xiaolong Liu − *Key Laboratory of Design and Assembly of Functional Nanostructures, Fujian Institute of Research on the Structure of Matter, Chinese Academy of Sciences, Fuzhou 350002, China;* ⓘ orcid.org/0000-0002-3096-4981; Email: xiaoloong.liu@gmail.com

Guojun Zhang − *Cancer Center and Department of Breast and Thyroid Surgery, Xiang'an Hospital of Xiamen University, School of Medicine, Fujian Key Laboratory of Precision Diagnosis and Treatment in Breast Cancer, Xiang'an Hospital of Xiamen University, School of Medicine, Xiamen Key Laboratory of Endocrine-Related Cancer Precision Medicine, Xiang'an Hospital of Xiamen University, School of Medicine, Department of Oncology, Xiang'an Hospital of Xiamen University, School of Medicine, and Cancer Research Center of Xiamen University, School of Medicine, Xiamen University, Xiamen 361100, China;* ⓘ orcid.org/0000-0001-5182-5887; Email: gjzhang@xah.xmu.edu.cn

Authors

Min Wei − *Cancer Center and Department of Breast and Thyroid Surgery, Xiang'an Hospital of Xiamen University, School of Medicine, Fujian Key Laboratory of Precision Diagnosis and Treatment in Breast Cancer, Xiang'an Hospital of Xiamen University, School of Medicine, Xiamen Key Laboratory of Endocrine-Related Cancer Precision Medicine, Xiang'an Hospital of Xiamen University, School of Medicine, and Xiamen Research Center of Clinical Medicine in Breast and Thyroid Cancers, Xiang'an Hospital of Xiamen University, School of Medicine, Xiamen University, Xiamen 361100, China*

Jingwen Bai − *Cancer Center and Department of Breast and Thyroid Surgery, Xiang'an Hospital of Xiamen University, School of Medicine, Fujian Key Laboratory of Precision Diagnosis and Treatment in Breast Cancer, Xiang'an Hospital of Xiamen University, School of Medicine, Xiamen Key Laboratory of Endocrine-Related Cancer Precision Medicine, Xiang'an Hospital of Xiamen University, School of Medicine, Xiamen Research Center of Clinical Medicine in Breast and Thyroid Cancers, Xiang'an Hospital of Xiamen University, School of Medicine, and Department of Oncology, Xiang'an Hospital of Xiamen University, School of Medicine, Xiamen University, Xiamen 361100, China*

Xiao Shen − *Cancer Center and Department of Breast and Thyroid Surgery, Xiang'an Hospital of Xiamen University, School of Medicine, Fujian Key Laboratory of Precision Diagnosis and Treatment in Breast Cancer, Xiang'an Hospital of Xiamen University, School of Medicine, Xiamen Key Laboratory of Endocrine-Related Cancer Precision*

Medicine, Xiang'an Hospital of Xiamen University, School of Medicine, and Xiamen Research Center of Clinical Medicine in Breast and Thyroid Cancers, Xiang'an Hospital of Xiamen University, School of Medicine, Xiamen University, Xiamen 361100, China

Kangliang Lou − *Cancer Center and Department of Breast and Thyroid Surgery, Xiang'an Hospital of Xiamen University, School of Medicine, Fujian Key Laboratory of Precision Diagnosis and Treatment in Breast Cancer, Xiang'an Hospital of Xiamen University, School of Medicine, Xiamen Key Laboratory of Endocrine-Related Cancer Precision Medicine, Xiang'an Hospital of Xiamen University, School of Medicine, and Xiamen Research Center of Clinical Medicine in Breast and Thyroid Cancers, Xiang'an Hospital of Xiamen University, School of Medicine, Xiamen University, Xiamen 361100, China*

Yiyang Gao − *Cancer Center and Department of Breast and Thyroid Surgery, Xiang'an Hospital of Xiamen University, School of Medicine, Fujian Key Laboratory of Precision Diagnosis and Treatment in Breast Cancer, Xiang'an Hospital of Xiamen University, School of Medicine, Xiamen Key Laboratory of Endocrine-Related Cancer Precision Medicine, Xiang'an Hospital of Xiamen University, School of Medicine, and Xiamen Research Center of Clinical Medicine in Breast and Thyroid Cancers, Xiang'an Hospital of Xiamen University, School of Medicine, Xiamen University, Xiamen 361100, China*

Ruichan Lv − *Engineering Research Center of Molecular and Neuro Imaging, Ministry of Education, School of Life Science and Technology, Xidian University, Xi'an 710071 Shanxi, China;* ⓘ orcid.org/0000-0002-6360-6478

Complete contact information is available at:
https://pubs.acs.org/10.1021/acsnano.3c00350

Author Contributions

[¶]Min Wei and Jingwen Bai contributed equally to this work.

Notes

The authors declare no competing financial interest.

REFERENCES

(1) Zhu, S. Y.; Yu, K. D. Breast Cancer Vaccines: Disappointing or Promising? *Front. Immunol.* **2022**, *13*, 828386.

(2) Moo, T. A.; Sanford, R.; Dang, C.; Morrow, M. Overview of Breast Cancer Therapy. *PET Clin.* **2018**, *13*, 339−354.

(3) McEvoy, M. P.; Landercasper, J.; Naik, H. R.; Feldman, S. Update of the American Society of Breast Surgeons Toolbox to Address the Lumpectomy Reoperation Epidemic. *Gland Surg.* **2018**, *7*, 536−553.

(4) Schulman, A. M.; Mirrielees, J. A.; Leverson, G.; Landercasper, J.; Greenberg, C.; Wilke, L. G. Reexcision Surgery for Breast Cancer:

An Analysis of the American Society of Breast Surgeons (Asbrs) Mastery (Sm) Database Following the Sso-Astro "No Ink on Tumor" Guidelines. *Ann. Surg. Oncol.* **2017**, *24*, 52−58.

(5) Jeevan, R.; Cromwell, D. A.; Trivella, M.; Lawrence, G.; Kearins, O.; Pereira, J.; Sheppard, C.; Caddy, C. M.; van der Meulen, J. H. Reoperation Rates after Breast Conserving Surgery for Breast Cancer among Women in England: Retrospective Study of Hospital Episode Statistics. *Bmj.* **2012**, *345*, e4505.

(6) Rosenthal, E. L.; Warram, J. M.; de Boer, E.; Basilion, J. P.; Biel, M. A.; Bogyo, M.; Bouvet, M.; Brigman, B. E.; Colson, Y. L.; DeMeester, S. R.; Gurtner, G. C.; Ishizawa, T.; Jacobs, P. M.; Keereweer, S.; Liao, J. C.; Nguyen, Q. T.; Olson, J. M.; Paulsen, K. D.; Rieves, D.; Sumer, B. D.; et al. Successful Translation of Fluorescence Navigation During Oncologic Surgery: A Consensus Report. *J. Nucl. Med.* **2016**, *57*, 144−150.

(7) Zheng, F.; Huang, X.; Ding, J.; Bi, A.; Wang, S.; Chen, F.; Zeng, W. NIR-I Dye-Based Probe: A New Window for Bimodal Tumor Theranostics. *Front. Chem.* **2022**, *10*, 859948.

(8) Lauwerends, L. J.; van Driel, P.; Baatenburg de Jong, R. J.; Hardillo, J. A. U.; Koljenovic, S.; Puppels, G.; Mezzanotte, L.; Löwik, C.; Rosenthal, E. L.; Vahrmeijer, A. L.; Keereweer, S. Real-Time Fluorescence Imaging in Intraoperative Decision Making for Cancer Surgery. *Lancet Oncol.* **2021**, *22*, e186−e195.

(9) Vahrmeijer, A. L.; Hutteman, M.; van der Vorst, J. R.; van de Velde, C. J.; Frangioni, J. V. Image-Guided Cancer Surgery Using Near-Infrared Fluorescence. *Nat. Rev. Clin. Oncol.* **2013**, *10*, 507−518.

(10) Hadjipanayis, C. G.; Stummer, W. 5-ALA and FDA Approval for Glioma Surgery. *J. Neurooncol.* **2019**, *141*, 479−486.

(11) Budner, O.; Cwalinski, T.; Skokowski, J.; Marano, L.; Resca, L.; Cwalina, N.; Kalinowski, L.; Hoveling, R.; Roviello, F.; Polom, K. Methylene Blue Near-Infrared Fluorescence Imaging in Breast Cancer Sentinel Node Biopsy. *Cancers (Basel)* **2022**, *14*, 1817.

(12) Wang, X.; Teh, C. S. C.; Ishizawa, T.; Aoki, T.; Cavallucci, D.; Lee, S. Y.; Panganiban, K. M.; Perini, M. V.; Shah, S. R.; Wang, H.; Xu, Y.; Suh, K. S.; Kokudo, N. Consensus Guidelines for the Use of Fluorescence Imaging in Hepatobiliary Surgery. *Ann. Surg.* **2021**, *274*, 97−106.

(13) Cherrick, G. R.; Stein, S. W.; Leevy, C. M.; Davidson, C. S. Indocyanine Green: Observations on Its Physical Properties, Plasma Decay, and Hepatic Extraction. *J. Clin. Invest.* **1960**, *39*, 592−600.

(14) Antaris, A. L.; Chen, H.; Cheng, K.; Sun, Y.; Hong, G.; Qu, C.; Diao, S.; Deng, Z.; Hu, X.; Zhang, B.; Zhang, X.; Yaghi, O. K.; Alamparambil, Z. R.; Hong, X.; Cheng, Z.; Dai, H. A Small-Molecule Dye for NIR-II Imaging. *Nat. Mater.* **2016**, *15*, 235−242.

(15) Tummers, Q. R.; Hoogstins, C. E.; Peters, A. A.; de Kroon, C. D.; Trimbos, J. B.; van de Velde, C. J.; Frangioni, J. V.; Vahrmeijer, A. L.; Gaarenstroom, K. N. The Value of Intraoperative Near-Infrared Fluorescence Imaging Based on Enhanced Permeability and Retention of Indocyanine Green: Feasibility and False-Positives in Ovarian Cancer. *PLoS One* **2015**, *10*, e0129766.

(16) Rodriguez, J. G. Z.; Grendar, J.; Jutric, Z.; Cassera, M. A.; Wolf, R. F.; Hansen, P. D.; Hammill, C. W. Evaluation of Indocyanine Green Fluorescence Imaging for Intraoperative Identification of Liver Malignancy. *Surg. Technol. Int.* **2021**, *39*, 85−90.

(17) Dang, X.; Bardhan, N. M.; Qi, J.; Gu, L.; Eze, N. A.; Lin, C.-W.; Kataria, S.; Hammond, P. T.; Belcher, A. M. Deep-Tissue Optical Imaging of Near Cellular-Sized Features. *Sci. Rep.* **2019**, *9*, 3873.

(18) Li, C.; Chen, G.; Zhang, Y.; Wu, F.; Wang, Q. Advanced Fluorescence Imaging Technology in the Near-Infrared-II Window for Biomedical Applications. *J. Am. Chem. Soc.* **2020**, *142*, 14789−14804.

(19) Antaris, A. L.; Chen, H.; Diao, S.; Ma, Z.; Zhang, Z.; Zhu, S.; Wang, J.; Lozano, A. X.; Fan, Q.; Chew, L.; Zhu, M.; Cheng, K.; Hong, X.; Dai, H.; Cheng, Z. A High Quantum Yield Molecule-Protein Complex Fluorophore for Near-Infrared II Imaging. *Nat. Commun.* **2017**, *8*, 15269.

(20) Starosolski, Z.; Bhavane, R.; Ghaghada, K. B.; Vasudevan, S. A.; Kaay, A.; Annapragada, A. Indocyanine Green Fluorescence in Second Near-Infrared (NIR-II) Window. *PLoS One* **2017**, *12*, e0187563.

(21) Yang, R. Q.; Wang, P. Y.; Lou, K. L.; Dang, Y. Y.; Tian, H. N.; Li, Y.; Gao, Y. Y.; Huang, W. H.; Zhang, Y. Q.; Liu, X. L.; Zhang, G. J. Biodegradable Nanoprobe for NIR-II Fluorescence Image-Guided Surgery and Enhanced Breast Cancer Radiotherapy Efficacy. *Adv. Sci.* **2022**, *9*, e2104728.

(22) Yang, Y.; Zhang, M.; Song, H.; Yu, C. Silica-Based Nanoparticles for Biomedical Applications: From Nanocarriers to Biomodulators. *Acc. Chem. Res.* **2020**, *53*, 1545−1556.

(23) Janjua, T. I.; Cao, Y.; Yu, C.; Popat, A. Clinical Translation of Silica Nanoparticles. *Nat. Rev. Mater.* **2021**, *6*, 1072−1074.

(24) Meola, T. R.; Abuhelwa, A. Y.; Joyce, P.; Clifton, P.; Prestidge, C. A. A Safety, Tolerability, and Pharmacokinetic Study of a Novel Simvastatin Silica-Lipid Hybrid Formulation in Healthy Male Participants. *Drug Delivery Transl. Res.* **2021**, *11*, 1261−1272.

(25) Lee, C.-H.; Cheng, S.-H.; Wang, Y.-J.; Chen, Y.-C.; Chen, N.-T.; Souris, J.; Chen, C.-T.; Mou, C.-Y.; Yang, C.-S.; Lo, L.-W. Near-Infrared Mesoporous Silica Nanoparticles for Optical Imaging: Characterization and in Vivo Biodistribution. *Adv. Funct. Mater.* **2009**, *19*, 215−222.

(26) Wang, W.; Wang, P.; Tang, X.; Elzatahry, A. A.; Wang, S.; Al-Dahyan, D.; Zhao, M.; Yao, C.; Hung, C.-T.; Zhu, X.; Zhao, T.; Li, X.; Zhang, F.; Zhao, D. Facile Synthesis of Uniform Virus-Like Mesoporous Silica Nanoparticles for Enhanced Cellular Internalization. *ACS Cent. Sci.* **2017**, *3*, 839−846.

(27) Häffner, S. M.; Parra-Ortiz, E.; Browning, K. L.; Jørgensen, E.; Skoda, M. W. A.; Montis, C.; Li, X.; Berti, D.; Zhao, D.; Malmsten, M. Membrane Interactions of Virus-Like Mesoporous Silica Nanoparticles. *ACS Nano* **2021**, *15*, 6787−6800.

(28) Matsunaga, Y.; Yamaoka, T.; Ohba, M.; Miura, S.; Masuda, H.; Sangai, T.; Takimoto, M.; Nakamura, S.; Tsurutani, J. Novel Anti-FOLR1 Antibody-Drug Conjugate Morab-202 in Breast Cancer and Non-Small Cell Lung Cancer Cells. *Antibodies (Basel)* **2021**, *10*, 6.

(29) Gajaria, P.; Kadu, V.; Patil, A.; Desai, S.; Shet, T. Triple Negative Breast Cancer: Expression of Folate Receptor Alpha in Indian Population. *Ann. Diagn. Pathol.* **2020**, *49*, 151598.

(30) Yee, C.; Alayed, Y.; Drost, L.; Karam, I.; Vesprini, D.; McCann, C.; Soliman, H.; Zhang, L.; Chow, E.; Chan, S.; Lee, J. Radiotherapy for Patients with Unresected Locally Advanced Breast Cancer. *Ann. Palliat. Med.* **2018**, *7*, 373−384.

(31) Lapierre, A.; Gourgou, S.; Brengues, M.; Quéro, L.; Deutsch, É.; Milliat, F.; Riou, O.; Azria, D. Tumour and Normal Tissue Radiosensitivity. *Cancer Radiother.* **2022**, *26*, 96−103.

(32) Xu, Y.; Dong, B.; Zhu, W.; Li, J.; Huang, R.; Sun, Z.; Yang, X.; Liu, L.; He, H.; Liao, Z.; Guan, N.; Kong, Y.; Wang, W.; Chen, J.; He, H.; Qiu, G.; Zeng, M.; Pu, J.; Hu, W.; Bao, Y.; et al. A Phase III Multicenter Randomized Clinical Trial of 60 Gy Versus 50 Gy Radiation Dose in Concurrent Chemoradiotherapy for Inoperable Esophageal Squamous Cell Carcinoma. *Clin. Cancer Res.* **2022**, *28*, 1792−1799.

(33) Zhang, Z.; Lu, M.; Chen, C.; Tong, X.; Li, Y.; Yang, K.; Lv, H.; Xu, J.; Qin, L. Holo-Lactoferrin: The Link between Ferroptosis and Radiotherapy in Triple-Negative Breast Cancer. *Theranostics* **2021**, *11*, 3167−3182.

(34) Ivanov, S. D.; Semenov, A. L.; Kovan'ko, E. G.; Yamshanov, V. A. Effects of Iron Ions and Iron Chelation on the Efficiency of Experimental Radiotherapy of Animals with Gliomas. *Bull. Exp. Biol. Med.* **2015**, *158*, 800−803.

(35) Lei, G.; Zhang, Y.; Koppula, P.; Liu, X.; Zhang, J.; Lin, S. H.; Ajani, J. A.; Xiao, Q.; Liao, Z.; Wang, H.; Gan, B. The Role of Ferroptosis in Ionizing Radiation-Induced Cell Death and Tumor Suppression. *Cell Res.* **2020**, *30*, 146−162.

(36) Dixon, S. J.; Lemberg, K. M.; Lamprecht, M. R.; Skouta, R.; Zaitsev, E. M.; Gleason, C. E.; Patel, D. N.; Bauer, A. J.; Cantley, A. M.; Yang, W. S.; Morrison, B., 3rd; Stockwell, B. R. Ferroptosis: An Iron-Dependent Form of Nonapoptotic Cell Death. *Cell* **2012**, *149*, 1060−1072.

(37) Yu, Y.; Yan, Y.; Niu, F.; Wang, Y.; Chen, X.; Su, G.; Liu, Y.; Zhao, X.; Qian, L.; Liu, P.; Xiong, Y. Ferroptosis: A Cell Death

Connecting Oxidative Stress, Inflammation and Cardiovascular Diseases. *Cell Death Discovery* **2021**, 7, 193.

(38) Li, J.; Cao, F.; Yin, H.-l.; Huang, Z.-j.; Lin, Z.-t.; Mao, N.; Sun, B.; Wang, G. Ferroptosis: Past, Present and Future. *Cell Death Dis.* **2020**, 11, 88.

(39) Ursini, F.; Maiorino, M. Lipid Peroxidation and Ferroptosis: The Role of GSH and GPX4. *Free Radic. Biol. Med.* **2020**, 152, 175−185.

(40) Matsumoto, K.; Saitoh, H.; Doan, T. L. H.; Shiro, A.; Nakai, K.; Komatsu, A.; Tsujimoto, M.; Yasuda, R.; Kawachi, T.; Tajima, T.; Tamanoi, F. Destruction of Tumor Mass by Gadolinium-Loaded Nanoparticles Irradiated with Monochromatic X-Rays: Implications for the Auger Therapy. *Sci. Rep.* **2019**, 9, 13275.

(41) Gamcsik, M. P.; Kasibhatla, M. S.; Teeter, S. D.; Colvin, O. M. Glutathione Levels in Human Tumors. *Biomarkers* **2012**, 17, 671−691.

(42) Lu, Y.; Yang, Y.; Gu, Z.; Zhang, J.; Song, H.; Xiang, G.; Yu, C. Glutathione-Depletion Mesoporous Organosilica Nanoparticles As a Self-Adjuvant and Co-Delivery Platform for Enhanced Cancer Immunotherapy. *Biomaterials* **2018**, 175, 82−92.

(43) Mindt, S.; Karampinis, I.; John, M.; Neumaier, M.; Nowak, K. Stability and Degradation of Indocyanine Green in Plasma, Aqueous Solution and Whole Blood. *Photochem. Photobiol. Sci.* **2018**, 17, 1189−1196.

(44) Michelet, F.; Guéguen, R.; Leroy, P.; Wellman, M.; Nicolas, A.; Siest, G. r. Blood and Plasma Glutathione Measured in Healthy Subjects by Hplc: Relation to Sex, Aging, Biological Variables, and Life Habits. *Clin. Chem.* **1995**, 41, 1509−1517.

(45) Liu, C.; Wang, D.; Zhang, S.; Cheng, Y.; Yang, F.; Xing, Y.; Xu, T.; Dong, H.; Zhang, X. Biodegradable Biomimic Copper/Manganese Silicate Nanospheres for Chemodynamic/Photodynamic Synergistic Therapy with Simultaneous Glutathione Depletion and Hypoxia Relief. *ACS Nano* **2019**, 13, 4267−4277.

(46) George, S.; Abrahamse, H. Redox Potential of Antioxidants in Cancer Progression and Prevention. *Antioxidants (Basel)* **2020**, 9, 1156.

(47) Bavi, O.; Cox, C. D.; Vossoughi, M.; Naghdabadi, R.; Jamali, Y.; Martinac, B. Influence of Global and Local Membrane Curvature on Mechanosensitive Ion Channels: A Finite Element Approach. *Membranes (Basel)* **2016**, 6, 14.

(48) Clough, T. J.; Jiang, L.; Wong, K.-L.; Long, N. J. Ligand Design Strategies to Increase Stability of Gadolinium-Based Magnetic Resonance Imaging Contrast Agents. *Nat. Commun.* **2019**, 10, 1420.

(49) Christenson, J. L.; Butterfield, K. T.; Spoelstra, N. S.; Norris, J. D.; Josan, J. S.; Pollock, J. A.; McDonnell, D. P.; Katzenellenbogen, B. S.; Katzenellenbogen, J. A.; Richer, J. K. Mmtv-Pymt and Derived Met-1 Mouse Mammary Tumor Cells As Models for Studying the Role of the Androgen Receptor in Triple-Negative Breast Cancer Progression. *Horm. Cancer* **2017**, 8, 69−77.

(50) Sousa, C.; Cruz, M.; Neto, A.; Pereira, K.; Peixoto, M.; Bastos, J.; Henriques, M.; Roda, D.; Marques, R.; Miranda, C.; Melo, G.; Sousa, G.; Figueiredo, P.; Alves, P. Neoadjuvant Radiotherapy in the Approach of Locally Advanced Breast Cancer. *ESMO Open* **2020**, 5, e000640.

(51) Raavi, V.; Perumal, V.; Paul, S. F. D. Potential Application of Γ-H2ax As a Biodosimetry Tool for Radiation Triage. *Mutat. Res. Rev. Mutat. Res.* **2021**, 787, 108350.

(52) Javadov, S. Mitochondria and Ferroptosis. *Curr. Opin. Physiol.* **2022**, 25, 100483.

(53) Friedmann Angeli, J. P.; Schneider, M.; Proneth, B.; Tyurina, Y. Y.; Tyurin, V. A.; Hammond, V. J.; Herbach, N.; Aichler, M.; Walch, A.; Eggenhofer, E.; Basavarajappa, D.; Rådmark, O.; Kobayashi, S.; Seibt, T.; Beck, H.; Neff, F.; Esposito, I.; Wanke, R.; Förster, H.; Yefremova, O.; et al. Inactivation of the Ferroptosis Regulator GPX4 Triggers Acute Renal Failure in Mice. *Nat. Cell Biol.* **2014**, 16, 1180−1191.

(54) Stockwell, B. R.; Friedmann Angeli, J. P.; Bayir, H.; Bush, A. I.; Conrad, M.; Dixon, S. J.; Fulda, S.; Gascón, S.; Hatzios, S. K.; Kagan, V. E.; Noel, K.; Jiang, X.; Linkermann, A.; Murphy, M. E.; Overholtzer, M.; Oyagi, A.; Pagnussat, G. C.; Park, J.; Ran, Q.; Rosenfeld, C. S.; et al. Ferroptosis: A Regulated Cell Death Nexus Linking Metabolism, Redox Biology, and Disease. *Cell* **2017**, 171, 273−285.

(55) Maishman, T.; Cutress, R. I.; Hernandez, A.; Gerty, S.; Copson, E. R.; Durcan, L.; Eccles, D. M. Local Recurrence and Breast Oncological Surgery in Young Women with Breast Cancer: The Posh Observational Cohort Study. *Ann. Surg.* **2017**, 266, 165−172.

(56) Kotovicz, F.; Mauad, T.; Saldiva, P. H. Clinico-Pathological Discrepancies in a General University Hospital in São Paulo, Brazil. *Clinics (Sao Paulo)* **2008**, 63, 581−588.

(57) Tang, R.; Coopey, S. B.; Buckley, J. M.; Aftreth, O. P.; Fernandez, L. J.; Brachtel, E. F.; Michaelson, J. S.; Gadd, M. A.; Specht, M. C.; Koerner, F. C.; Smith, B. L. A Pilot Study Evaluating Shaved Cavity Margins with Micro-Computed Tomography: A Novel Method for Predicting Lumpectomy Margin Status Intraoperatively. *Breast J.* **2013**, 19, 485−489.

(58) Wang, Z.; Chen, M.; Liu, J. J.; Chen, R. H.; Yu, Q.; Wang, G. M.; Nie, L. M.; Huang, W. H.; Zhang, G. J. Human Serum Albumin Decorated Indocyanine Green Improves Fluorescence-Guided Resection of Residual Lesions of Breast Cancer in Mice. *Front. Oncol.* **2021**, 11, 614050.

(59) Zhang, Y. Q.; Liu, W. L.; Luo, X. J.; Shi, J. P.; Zeng, Y. Z.; Chen, W. L.; Huang, W. H.; Zhu, Y. Y.; Gao, W. L.; Li, R. H.; Ming, Z. H.; Zhang, L. X.; Yang, R. Q.; Wang, J. Z.; Zhang, G. J. Novel Self-Assembled Multifunctional Nanoprobes for Second-Near-Infrared-Fluorescence-Image-Guided Breast Cancer Surgery and Enhanced Radiotherapy Efficacy. *Adv. Sci.* **2023**, 10, e2205294.

(60) Li, B.; Zhao, M.; Feng, L.; Dou, C.; Ding, S.; Zhou, G.; Lu, L.; Zhang, H.; Chen, F.; Li, X.; Li, G.; Zhao, S.; Jiang, C.; Wang, Y.; Zhao, D.; Cheng, Y.; Zhang, F. Organic NIR-II Molecule with Long Blood Half-Life for in Vivo Dynamic Vascular Imaging. *Nat. Commun.* **2020**, 11, 3102.

(61) Hofmeyer, S.; Pekár, G.; Gere, M.; Tarján, M.; Hellberg, D.; Tot, T. Comparison of the Subgross Distribution of the Lesions in Invasive Ductal and Lobular Carcinomas of the Breast: A Large-Format Histology Study. *Int. J. Breast Cancer* **2012**, 2012, 436141.

(62) Shah, C.; Bauer-Nilsen, K.; McNulty, R. H.; Vicini, F. Novel Radiation Therapy Approaches for Breast Cancer Treatment. *Semin. Oncol.* **2020**, 47, 209−216.

(63) Chakraborty, S.; Chatterjee, S. Adjuvant Radiation Therapy in Breast Cancer: Recent Advances & Indian Data. *Indian J. Med. Res.* **2021**, 154, 189−198.

(64) Čepelak, I.; Dodig, S.; Dodig, D. Ferroptosis: Regulated Cell Death. *Arh. Hig. Rada. Toksikol.* **2020**, 71, 99−109.

(65) Bai, J. W.; Chen, M. N.; Wei, X. L.; Li, Y. C.; Lin, H. Y.; Chen, M.; Li, J. W.; Du, C. W.; Man, K.; Zhang, G. J. The Zinc-Finger Transcriptional Factor Slug Transcriptionally Downregulates Erα by Recruiting Lysine-Specific Demethylase 1 in Human Breast Cancer. *Oncogenesis* **2017**, 6, e330.